INTERNATIONAL JOURNAL OF GEOGRAPHICAL INFORMATION SCIENCE
https://doi.org/10.1080/13658816.2023.2224421

Taylor & Francis
Taylor & Francis Group

RESEARCH ARTICLE

Check for updates

Using airborne lidar and machine learning to predict visibility across diverse vegetation and terrain conditions

Katherine A. Mistick[a], Michael J. Campbell[a], Matthew P. Thompson[b] and Philip E. Dennison[a]

[a]Department of Geography, University of Utah, Salt Lake City, UT, USA; [b]Missoula Fire Sciences Laboratory, Rocky Mountain Research Station, Missoula, MT, USA

ABSTRACT

Visibility analyses, used in many disciplines, rely on viewshed algorithms that map locations visible to an observer based on a given surface model. Mapping continuous visibility over broad extents is uncommon due to extreme computational expense. This study introduces a novel method for spatially-exhaustive visibility mapping using airborne lidar and random forests that requires only a sparse sample of viewsheds. In 24 topographically and vegetatively diverse landscapes across the contiguous US, 1000 random point viewsheds were generated at four different observation radii (125 m, 250 m, 500 m, 1000 m), using a 1 m resolution lidar-derived digital surface model. Visibility index – the proportion of visible area to total area – was used as the target variable for site-scale and national-scale modeling, which used a diverse set of 146 terrain- and vegetation-based 10 m resolution metrics as predictors. Variables based on vegetation, especially those based on local neighborhoods, were more important than those based on terrain. Visibility at shorter distances was more accurately estimated. National-scale models trained on a wider range of vegetation and terrain conditions resulted in improved R^2, although at some sites error increased compared to site-scale models. Results from an independent test site demonstrate potential for application of this methodology to diverse landscapes.

ARTICLE HISTORY
Received 28 February 2023
Accepted 7 June 2023

KEYWORDS
Viewshed; visibility; lidar; random forest

1. Introduction

The ability to estimate landscape visibility from a particular vantage point has great value in many disciplines (Inglis *et al.* 2022), including but not limited to archaeology (Fisher *et al.* 1997, Lake *et al.* 1998, Llobera 2003, O'Driscoll 2017, Schirru and Castangia 2022), ecology (Aben *et al.* 2018, Parsons *et al.* 2020, Wyse *et al.* 2022, Zong *et al.* 2022), landscape and urban planning (Bartie *et al.* 2011, Chamberlain and Meitner 2013, Yu *et al.* 2016, Vukomanovic *et al.* 2018) and emergency response (Pompa-Garcia 2010, Sivrikaya *et al.* 2013, Kucuk *et al.* 2017, Mistick *et al.* 2022). Archaeological studies have demonstrated how visibility may have influenced the

CONTACT Katherine Mistick katherine.mistick@utah.edu
© 2023 Informa UK Limited, trading as Taylor & Francis Group

settlement patterns of historical peoples and can provide insight into the role that built features may have played (Fisher *et al.* 1997, Jones 2006, Schirru and Castangia 2022). Visibility plays a key role in the evaluation of animal habitat suitability and behavioral patterns (Aben *et al.* 2018, Parsons *et al.* 2020). Visibility analyses can also provide useful insight into maximizing esthetically pleasing views (Chamberlain and Meitner 2013, Yu *et al.* 2016). Wildland firefighters can use visibility analyses to evaluate areas that may promote or hinder situational awareness (Mistick *et al.* 2022). Previous studies have also focused on areas of increased visibility (eg how increasing views results in increased home sale prices (Sander and Polasky 2009)) and areas of decreased visibility (eg prey animals seeking concealment (Olsoy *et al.* 2015) or minimizing views of natural resource extraction (Franklin and Ray 1994)).

Traditional visibility studies have relied on photography for quantifying visual impacts such as clear cutting (Dean and Lizarraga-Blackard 2007, Palmer 2008). However, current visibility analyses typically rely on the use of point-based viewsheds to quantify how much of the landscape is visible to an observer (Fisher et al. 1997, Wheatley and Gillings 2000, Llobera 2003, Inglis et al. 2022). Most commonly, viewshed algorithms use a digital terrain model (DTM) to perform a line-of-sight calculation from a particular vantage point to determine whether terrain features are obstructing sightlines to all surrounding locations across a landscape. This process results in a binary viewshed map distinguishing between visible and obscured areas; however, viewsheds based solely on terrain features provide an overly-optimistic estimate of proportional visibility (Guth 2009, Starek et al. 2020). For example, using a DTM to assess visibility in a forested area may result in unrealistically high visibility estimates due to the omission of significant vegetative obstructions to lines of sight. Airborne laser scanner (ALS) data, also known as airborne lidar, has been used in visibility assessments to provide even greater three-dimensional landscape detail (Hindsley *et al.* 2013, Murgoitio *et al.* 2013). With the increasing availability and use of ALS data, digital surface models (DSMs) are increasingly being used in viewshed analyses to account for vegetation obstructions to visibility in addition to terrain, providing much more realistic and conservative visibility estimates (Inglis *et al.* 2022, Mistick *et al.* 2022).

Visibility can be reduced to a fractional value using a visibility index (VI) representing the proportion of visible area from a given location (Franklin and Ray 1994, Mistick *et al.* 2022). Figure 1 shows a conceptual example of how a VI is calculated. It begins with a binary viewshed, generated from a single observer within a given radius. Within that radius VI is calculated as a ratio between the area that is visible to that observer and the area of the entire radius-defined buffer around that observer. Using Figure 1 as an example, a VI of 0.09 can be interpreted as 9% of the surrounding landscape being visible to the observer (or, conversely, 9% of the landscape having a view of the observer, as the relationship is assumed to be reciprocal).

Previous work has demonstrated the value of using multiple viewshed calculations to understand visibility trends across larger areas. Cumulative viewshed methods allow for broader understanding of landscape-scale visibility by incorporating multiple observer points into the calculation, which improves upon the single-observer, binary viewshed approach by defining how visible areas are according to the number of

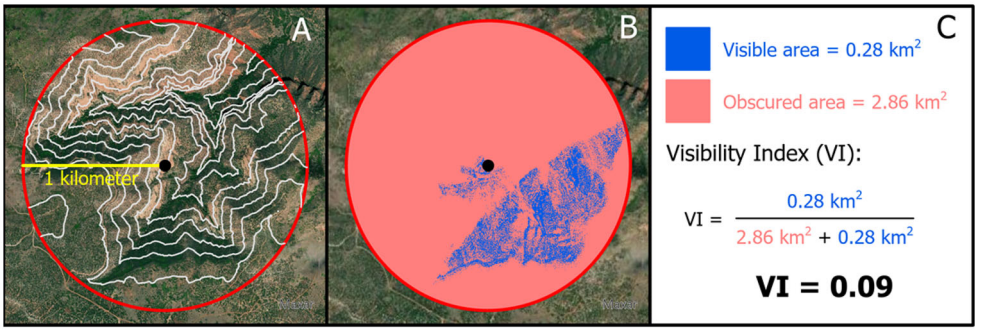

Figure 1. Example of a point-based viewshed calculated within a 1 km buffer on a landscape with varied terrain and vegetation. (A) A red circle with 1 km radius within which a viewshed is calculated from the central black observer point. White contours at a 50 m interval represent the DTM, and the aerial base image shows varying vegetation cover. (B) Visible area (blue) and obscured area (red), used in the (C) calculation of the visibility index (VI).

observer points that are able to view them (Wheatley 1995, Llobera 2003, Tabik *et al.* 2013, Aben *et al.* 2018, Inglis *et al.* 2022). Mapping visibility across entire landscapes requires calculating viewsheds from many points (Lake *et al.* 1998, Tabik *et al.* 2013, Zhao *et al.* 2013). Whether used for point-based visibility analyses or calculating VI, viewshed analysis methods relying on line-of-sight calculations are computationally expensive (van Kreveld 1996, Chao *et al.* 2011, Zhao *et al.* 2013, Qarah 2020).

If computational complexity issues can be resolved, mapping visibility across entire landscapes could provide important, spatially-explicit insight into areas on the landscape that promote or hinder visibility. For example, an ecologist could use a VI map to identify potential habitat preferences, or a wildland firefighter could identify locations to place a lookout. However, mapping VI in a spatially-exhaustive (pixel-by-pixel) manner over large areas would require the generation of a number of viewsheds equal to the number of pixels, potentially requiring immense computational power and lengthy processing times (Franklin and Ray 1994). For example, mapping visibility across the US state of Utah ($2.2 \times 10^5\,km^2$) at a spatial resolution of 30 m would require the computation of over 244 million viewsheds. Even if each viewshed only took one second to process, such an analysis would take nearly eight years to process sequentially.

Significant advancements have been made in speeding up visibility calculations through the introduction of new algorithms (Franklin and Ray 1994, Fishman *et al.* 2009, Tabik *et al.* 2015, Sahraoui *et al.* 2018), the use of advanced hardware such as GPUs (Gao *et al.* 2011, Stojanovic and Stojanovic 2013, Zhao *et al.* 2013, Cauchi-Saunders and Lewis 2015) and the total restructuring of data in combination with advanced hardware (Sanchez-Fernandez *et al.* 2021). Sanchez-Fernandez *et al.* (2021) produced total viewshed maps (akin to a VI map, but without normalization to the total area considered) with significant improvement in processing speed. Their algorithm provides an efficient technique for mapping visibility; however, it has only been tested on bare-earth terrain conditions, relies heavily on advanced hardware and software and requires the calculation of visibility from every possible point of view in a given area.

Rather than map visibility from every possible viewing perspective in a landscape, a machine learning algorithm may be able to map visibility using a comparably small subset of viewsheds to train a predictive model. Given our understanding of what terrain and vegetation features tend to promote or hinder visibility, a machine learning algorithm may be able to statistically link these features to sample viewsheds, enabling the prediction of visibility in unsampled areas and mapping visibility in a much more computationally-efficient manner. For example, high relative topographic position promotes visibility, while the presence of tall vegetation in one's surroundings hinders visibility. Considering that these landscape features can be readily mapped using a variety of data sources, including data derived from ALS as well as other sources (Farr and Kobrick 2000, Homer *et al.* 2012, Karlson *et al.* 2015, Vogeler *et al.* 2018, Potapov *et al.* 2021), perhaps a sparse sample of viewsheds can be used to drive a machine learning model that predicts visibility based on these features. Provided that such a model had sufficient predictive power, visibility could be mapped across entire areas much more efficiently than having to generate a computationally-expensive viewshed from every pixel location.

Using this sample-based viewshed approach, Zong *et al.* (2021, 2022) used random forests to model ALS-derived, fine-scale visibility trained with terrestrial laser scanner (TLS)-derived visibility. While their study demonstrated an impressive capacity to map VI using machine learning, there were a few limitations that prevent broad applicability. First, their approach relies on the collection of TLS data to calibrate and validate VI predictions, making this method only applicable in areas where TLS data exist or can be collected. Second, their VI calculations are inherently local, meaning they only estimate proportional visibility within the spatial extent of a single pixel (35×35 m). While this may be a useful scale for the wildlife application focus of their study, the ability to apply this technique to disciplines requiring broader-scale visibility estimates is limited. Third, their study was limited to a single study area, so the extent to which this approach could be more broadly applied remains unknown.

Given the importance and widespread use of visibility as a critical landscape metric in a variety of disciplines, there remains a need for an efficient algorithm to map visibility in a spatially explicit and exhaustive manner. The main objective of this study was to develop a new, computationally-efficient approach for mapping proportional visibility, in the form of VI, across entire landscapes using ALS and machine learning that relies only on a sparse sample of viewsheds. Our secondary objectives are as follows:

(1) To assess the extent to which visibility derived from a high-resolution surface model can be approximated by coarser resolution landscape information.
(2) To compare accuracies of models built within a specific area (ie 'site-scale' models) to models built across a diversity of areas (ie 'national-scale' models).
(3) To evaluate the effects of local terrain and vegetation conditions on VI predictive accuracies.
(4) To determine which among a suite of landscape-scale, lidar-derived terrain and vegetation metrics have the greatest influence on visibility.

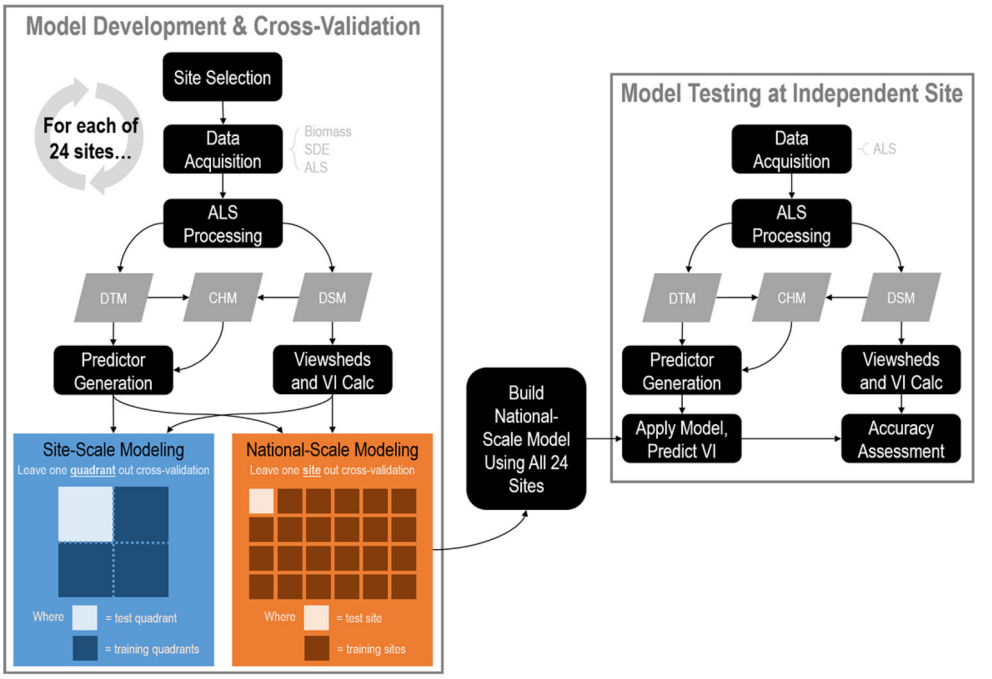

Figure 2. Flowchart summarizing the methodology used in this study.

We propose a random forest modeling approach that relies solely on ALS data to estimate VI at four viewing radii and at two scales: (1) site-scale and (2) national-scale. Site-scale modeling benefits from being tailored to site-specific landscape conditions, whereas national-scale modeling benefits from the incorporation of more diverse landscape conditions to yield broadly-applicable landscape-visibility relationships. Our approach has the potential to map VI across diverse landscapes and should be applicable to naturally-vegetated areas across the contiguous US. Given broad, multidisciplinary interest in visibility, this model has the potential to benefit a variety of research and applications currently limited by the computational cost of traditional visibility analysis.

2. Materials and methods

The methods used in this study are summarized in Figure 2. There were two main steps in our procedure: (1) model development and cross-validation; and (2) model testing at an independent site. In the first step, 24 study sites were selected, within which ALS data were used to generate sample viewsheds and a suite of terrain and vegetation predictor layers. VI was calculated from each viewshed and used to train and validate random forest models for predicting VI at site- and national-scales. In the second step, the national-scale model was used to predict VI at an independent test site, the accuracy of which was assessed using ALS-driven VI calculations.

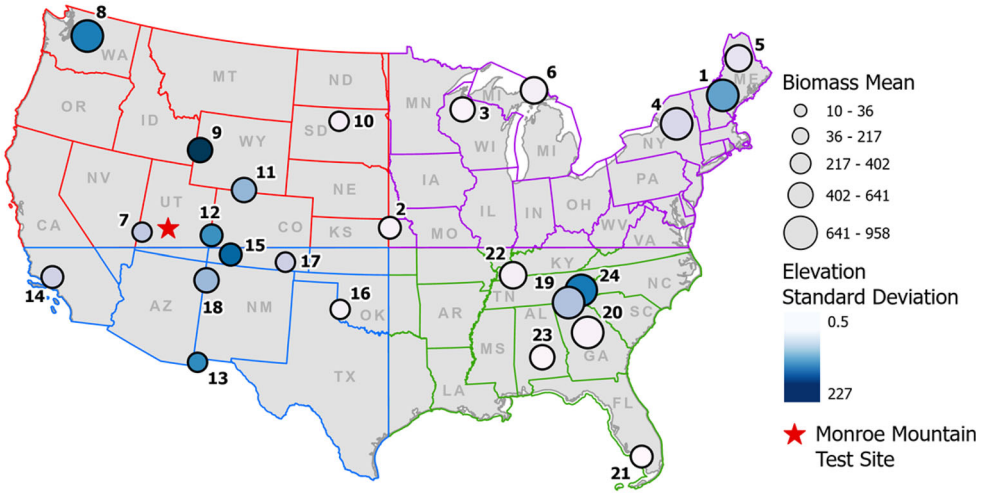

Figure 3. Training and validation sites used for modeling labeled by site number (Table A4). To display vegetative and topographic variability, points are sized by mean aboveground biomass and colored by standard deviation elevation (SDE). The red star represents the location of the Monroe Mountain test site in Utah, USA. Quadrant borders are colored geographically (NE = purple, SE = green, SW = red, NW = blue).

2.1. Site selection

To test the extent to which visibility can be modeled across a variety of landscapes, 24 study sites were selected to capture a broad range of vegetation and terrain conditions. Only naturally vegetated (non-developed, non-farmed) landscapes were selected for this study, based on MODIS MCD12Q1 land cover data (Friedl and Sulla-Menashe 2019), with fewer than ten structures per square kilometer according to Microsoft's building footprints (Microsoft 2018). Selected sites were required to be completely encompassed by US Geological Survey 3D Elevation Program (3DEP) Quality Level 1 (QL1) or 2 (QL2) ALS data extents (Sugarbaker et al. 2014) and free from any disturbances that occurred after data collection (according to LANDFIRE's historical disturbance map) (LANDFIRE Historical Disturbance 2023).

To ensure an appropriate geographical spread of study sites, the contiguous US was divided into four quadrants (NE, SE, SW and NW) (Figure 3). Within each quadrant, the sample_nc() function from the R (version 4.2.3) package sgsR (version 1.4.2) (Goodbody *et al.* 2023) was used to generate an initial set of 5 km × 5 km potential study sites. The algorithm, based on the work of Melville and Stone (2016), subdivides *n*-dimensional variable space into *m* clusters. It then identifies centroids within each cluster, with the intent of capturing a wide range of variability in the resulting sample. Mean aboveground biomass (Mg/ha) (from Spawn *et al.* 2020) and the standard deviation of elevation (SDE) (from PRISM Climate Group 2022) were calculated at potential sites to capture variation in both abundance (eg cover, height, density) of vegetation and variability in terrain. We created six clusters ($m = 6$) within each of the four US quadrants, driven by a combination of mean biomass and SDE ($n = 2$). This resulted in 24 categories of terrain and vegetation conditions (eg high-biomass/low-SDE, low-biomass/high-SDE, etc.).

Within each of these 24 categories, we placed five samples, representing potential study sites. Sites were then manually scored based on lidar quality and collection date, presence of developed or agricultural land and diversity and abundance of vegetation, with the goal of giving a higher ranking to sites with higher point density and more recently-collected ALS, lower proportions of developed or agricultural land cover and higher diversity of vegetation types. From each category, the highest ranked site was selected resulting in 24 final sites representing a wide range of geographic locations, mean biomass and SDE values (Figure 3).

2.2. Data acquisition

ALS data were used to generate DTMs, DSMs and canopy height models (CHMs) at each of the 24 sites and the additional test site (described in Section 2.3.2). All lidar data came from USGS 3DEP (Sugarbaker et al. 2014); see Table A1 for dataset details. Point clouds were processed into surface products using LAStools (version 230330 (academic), Isenburg 2019). DTMs were interpolated using the las2dem() function in LAStools, which generates a gridded representation of a triangulated irregular network built from lidar points classified as representing the ground surface. DSMs were interpolated using the first returns, representing the highest aboveground surface that the lidar pulses interacted with (eg treetops). CHMs were calculated as the difference between DSMs and DTMs. All models were generated at 1 m resolution (Figure 4).

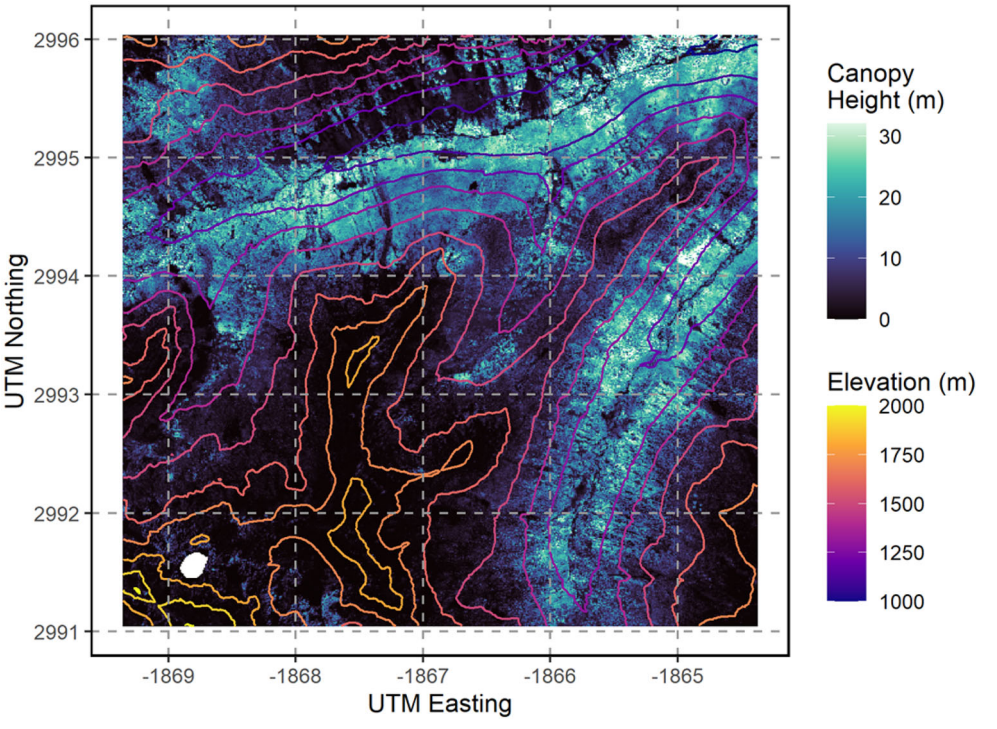

Figure 4. An example site (site 8) in Washington state (Figure 3) showing lidar-derived elevation (contours) and canopy height models (shading). UTM coordinates are provided in kilometers and represent zone 10, based on the North American Datum of 1983.

2.3. Modeling

To build a database of training and validation data, 1000 random points were generated within each site, with a restriction that points could not fall within 1 km of the site edge to ensure edges did not affect visibility calculations. From each point, viewsheds were generated and VI was calculated for four different observation radii: 125 m, 250 m, 500 m, 1000 m. Considering four radii allowed for comparison between short range (125 m), intermediate range (250 – 500 m) and long range (1000 m) visibility. Although humans can see distances beyond 1000 m, we chose these distances to balance computational expense with capturing a range of visibility scales. Viewsheds were computed using ArcGIS Pro's (version 3.1) Geodesic Viewshed tool (ESRI 2022a), using a Windows Server (384 GB memory) with Nvidia Tesla T4 graphics processing unit (320 tensor cores, 16 GB of memory). A sample of 1000 viewsheds represents a just 0.004% of the total viewsheds that would be necessary to map visibility in a spatially-exhaustive manner at each site. The lidar-derived 1 m DSM was used as the surface over which viewsheds were calculated to ensure that VI values represented visibility with a high degree of precision and to take into account the structure of both terrain and vegetation (Mistick *et al.* 2022).

Visibility was modeled at the site scale (trained and validated within each site) and at the national scale (trained and validated across sites). Site-scale modeling provides a sense of how well visibility could be estimated in local-scale studies, tailored to local terrain and vegetation conditions. For example, in topographically-diverse, sparsely-vegetated areas, terrain might be the dominant feature dictating visibility. Conversely, in densely-forested flat areas, vegetation structure would play a dominant role. National-scale modeling, on the other hand, produces a singular model capable of predicting visibility across all sites. Modeling was done using random forests from the ranger package in R (version 0.14.1) (Wright *et al.* 2022). Random forests are an ensemble machine learning technique frequently used in remote sensing and geographic information science (GIS) (Belgiu and Drăguţ 2016, Zhang *et al.* 2022) for classification and regression tasks such as land cover classification (Belgiu and Drăguţ 2016, McPartland *et al.* 2019), vegetation structure and disturbance mapping (Campbell *et al.* 2020, 2021), hazard susceptibility mapping (Chapi *et al.* 2017, Zhang *et al.* 2022) and ecosystem services (Hakkenberg *et al.* 2018, Otgonbayar *et al.* 2019), among many applications.

2.3.1. Variables

VI served as the target (ie 'dependent') variable for modeling and was calculated according to Equation (1):

$$\mathrm{VI} = \frac{A_V}{A_T} \tag{1}$$

where A_V is the visible area, and A_T is the total area over which the viewshed was calculated. One hundred and forty-six predictor (ie 'independent') variables were broadly categorized as terrain-based (DTM-derived) or vegetation-based (CHM-derived) (Table 1). Table 1 summarizes predictor categories; see Table A2 in Appendix A for full variable

Table 1. Summary of predictor variable categories.

Predictor	Description	Scope(s)	Type
Elevation[a]	Elevation value derived from 10 m DTM	Local, focal	Terrain
Slope[a]	Rate of change of elevation (steepness) derived from 10 m DTM	Local, focal	Terrain
Slope derivative[a]	Rate of change of slope derived from 10 m DTM	Local, focal	Terrain
Aspect sine[a]	The degree of 'east-ness' where a maximum value of 1 indicates east-facing and a minimum value of −1 indicates west-facing.	Local, focal	Terrain
Aspect cosine[a]	The degree of 'north-ness' where a maximum value of 1 indicates north-facing and a minimum value of −1 indicates south-facing.	Local, focal	Terrain
Slope-aspect sine[a]	The product of slope and aspect sine, designed to capture 'east-ness', while down-weighting relatively flat areas, and enhancing relatively steep areas.	Local, focal	Terrain
Slope-aspect cosine[a]	The product of slope and aspect cosine, designed to capture 'north-ness', while down-weighting relatively flat areas, and enhancing relatively steep areas.	Local, focal	Terrain
Curvature[a]	Curvature calculated on the 10 m DTM on a pixel-by-pixel basis according to the eight surrounding neighbors	Local, focal	Terrain
Curvature profile	Curvature in the direction of maximum slope	Local	Terrain
Curvature plan	Curvature in the direction perpendicular to maximum slope	Local	Terrain
Topographic position index (TPI)[b]	Relative elevation, derived according to an annulus, surrounding a point, with defined inner and outer radii (Weiss 2001)	Focal	Terrain
Canopy cover (CC)[a]	Metric describing vegetation density, calculated as the percentage of 1 m pixels with vegetation heights over 2 m within aggregated 10 m pixel area	Local, focal	Vegetation
Canopy height (CH)[a]	Height of vegetation above the surface, derived from 10 m CHM.	Local, focal	Vegetation
Segmented canopy height[c]	Canopy height segmentation using Segment Mean Shift (ESRI 2022b) to group pixels into similar height segments	Zonal	Vegetation
Segmented canopy cover[d]	Canopy cover segmentation using Segment Mean Shift (ESRI 2022b) to group pixels into similar canopy cover segments	Zonal	Vegetation
Distance to forest	Distance to a canopy height segment with a vegetation height greater than or equal to 2 m	Global	Vegetation
Distance to clearing	Distance to a canopy height segment with a vegetation height less than 2 m	Global	Vegetation

Notes: Predictors were generated using Spatial Analyst functions in the ArcPy Python (version 3.9.11) library. For more detailed information see Table A2 in Appendix A.
[a]Includes additional variables representing the mean and standard deviation of the respective variable within a radius of x pixels for x in [2, 4, 6, 8, 16 and 32].
[b]Includes variables with outer radii of x pixels for x in [2, 4, 6, 8, 16 and 32] where inner radius $= x/2$.
[c]Includes the mean, standard deviation, segment size and segment compactness of the variable.
[d]Includes the mean and standard deviation of the variable.

descriptions. This set of predictor variables was aimed at capturing the landscape-level characteristics that promote or hinder visibility.

Some of these features are inherently local, describing a terrain and vegetation characteristic that occurs within each pixel individually (eg elevation, slope, canopy cover, canopy height). Other features are focal, describing terrain and vegetation characteristics that occur within neighborhoods of varying size surrounding each pixel (eg topographic position index, mean canopy cover within pixel radii of 2, 4, 6, 8, 16 and 32). A third subset of features are zonal, which rely on the image segmentation of vegetation height and canopy cover data to produce polygons representing areas of

similar vegetation structure (eg mean segment canopy height and cover). And lastly, some features are global, describing landscape characteristics in a manner that evaluates the full extent of the site simultaneously (eg distance to forest and distance to clearing).

Predictor variables were generated at 10 m spatial resolution to determine if high resolution visibility (based on 1 m DSM) can be modeled using coarser landscape information. Given the wide availability of 10 m DTMs in the US and potential to use global remote sensing data to generate 10 m vegetation height maps (eg Lang *et al.* 2019), this resolution also provides insight into the potential capacity to predict VI in areas where ALS data have not been collected.

2.3.2. Model tuning

Both site-scale and national-scale models were tuned, using the tuneRanger package (version 0.5) (Probst *et al.* 2019), for three hyperparameters: *mtry*, *minimum node size* and *sample fraction*. *Mtry* is the number of predictor variables that are considered when splitting a node (Wright *et al.* 2022). Larger *mtry* values will increase the likelihood that the same set of more influential predictor variables will be driving the growth of decision trees, potentially resulting in more similar predictions among trees. Smaller *mtry* values may result in a greater diversity of trees, though potentially may result in the inclusion of less meaningful predictor variables. *Minimum node size* defines the minimum number of observations that can occupy a node, which implicitly defines the depth of decision trees within the forest. For example, a larger *minimum node size* would result in a shallower forest since nodes are required to have more observations and may lead to underfitting, whereas a small *minimum node size* allows the forest to grow deeper by allowing fewer observations in each node, though potentially at the expense of overfitting. *Sample fraction* defines the number of observations to sample in each tree as a proportion of total samples. For example, a *sample fraction* of 1 would sample 100% of observations for each tree, whereas a *sample fraction* of 0.75 would sample 75% of observations at each tree.

2.3.3. Site-scale modeling

Site-scale modeling was done within each of the 24 sites, at all four radii of interest (125, 250, 500 and 1000 m), using four-fold spatial cross-validation. Each site was divided into four geographical folds, where points within three folds were used to train a model and points within the remaining fold were left out for validation. This approach was taken to reduce the influence of spatial autocorrelation on the perception of model performance by ensuring that validation points did not spatially overlap with training points (Roberts *et al.* 2017). Models were tuned per-site and per-radius for a total of 96 sets of hyperparameters (Table A3). Each model was trained and predictions were generated in parallel using 30 CPU threads. Model performance was assessed across all validation folds, per-site and per-radius, according to the coefficient of determination (R^2) between predicted and observed VI, which characterizes the degree to which predictions explain variance in observations and quantifies correlation between the predicted and observed. Performance was also assessed according to the

normalized root mean square error (nRMSE), which characterizes average proportional predictive error relative to the range of observations, as follows:

$$nRMSE = \frac{\sqrt{\sum_{i=1}^{k} \frac{(\hat{y}_i - y_i)^2}{k}}}{y_{max} - y_{min}} \quad (2)$$

Where $\hat{y}_1$, $\hat{y}_2 \ldots \hat{y}_k$ are predicted VI values, y_1, y_2, … y_k are observed VI values, k is the total number of observations, y_{max} is the maximum observed VI and y_{min} is the minimum observed VI. nRMSE was selected over RMSE to allow for more direct comparison between predictive error of models of different visibility radii or between models of different scope (eg site-scale or national-scale). Performance metrics (R^2 and nRMSE) for each site at each visibility radius were compared to site characteristics (biomass, SDE, average observed VI), using Pearson's r to determine if significant correlations existed and understand potential drivers of VI predictive capacity.

2.3.4. National-scale modeling

National-scale VI modeling was implemented using a 'leave one site out' cross-validation technique where 96 models were built (24 sites × 4 radii) with each site left out once for validation. Model tuning, training and prediction were done in parallel using 30 CPU threads. Models were tuned per-radius, providing a more robust accounting of ideal hyperparameters. A *minimum node size* of 2 and *sample fraction* of 0.89 were consistent across radii, however *mtry* varied across radii with a value of 31 for 125 m, 43 for 250 m, 58 for 500 m and 56 for 1000 m. Model performance (R^2 and nRMSE) was assessed at each radius, for each of the 24 models, according to the validation data. As was done at the site-scale, Pearson's r was used to determine if significant correlations existed between performance metrics and site characteristics.

In the interest of gaining an unbiased demonstration of national-scale model performance across a larger area that was not included in the training and validation data, we selected Monroe Mountain, Utah, as an independent test area (Figure 3). The test site has diversity of topography and vegetation, is largely uninhabited and is a USDA Forest Service management unit within the Fishlake National Forest. ALS data were collected over the entire unit in 2016. The test site covers 742 km^2, just over 1.2 times the combined area covered by all 24 training and validation sites. For testing, 1000 points were randomly generated within the test site, again ensuring that points did not fall within 1 km of the study area's edge to avoid edge effects. This process also excluded areas within 1 km of any open water features, including reservoirs and lakes, to make sure that these relatively flat features did not artificially inflate VI. Viewsheds calculated from all 1000 points were used to test the final national-scale model, which was trained, per-radius, using all points from all 24 5 km × 5 km sites. Model predictions were mapped, per 10 m pixel, across the entire site using the terra R package (version 1.7-18) (Hijmans *et al.* 2022). Predicted VI was compared to observed VI calculated from the 1000 viewsheds with model performance assessed according to R^2 and nRMSE. To assess the extent to which the national model may or may not have accounted for Monroe Mountain's unique geography, we generated a

Table 2. Median site- and national-scale metrics at four visibility radii.

Visibility radius (m)	Median site-scale R^2	Median site-scale nRMSE	Median national-scale R^2	Median national-scale nRMSE
125	0.73	0.07	0.78	0.08
250	0.65	0.08	0.75	0.09
500	0.55	0.09	0.68	0.10
1000	0.62	0.10	0.59	0.12

subsequent random forest-driven model to explain prediction error (predicted – observed VI) as a function of the local terrain and vegetation features.

3. Results

Viewshed processing took an average of 7 s per point for all points used in training and validating the site- and national-scale models, for a total of nearly 47 h of processing. The Monroe Mountain viewsheds took an average of 23 s per point, owing to the larger processing extent, for a total of 6.4 h of processing. In contrast, the largest, most complex random forest model took 17 s to train, and only 40 min to predict VI values for every pixel within the test site. Based on viewshed processing times, producing a map of visibility for Monroe Mountain at 10 m point spacing would take over 5.4 years if processed sequentially (23 s/viewshed for 7.42 million pixels) using the ArcGIS Geodesic Viewshed tool, meaning our modeling technique was over 70,000 times faster for the test site.

3.1. Site-scale modeling

Site-scale models had a median R^2 of 0.64 across all models. Medians are reported rather than means due to the skewness of the distributions of performance metrics. Smaller radii models tended to produce higher R^2 values than larger radii models (Table 2; Figure 5(A)), suggesting that VI was more accurately modeled at shorter distances than that at longer distances. See Table A4 for per-site model performance and descriptive variables (eg biomass, average observed VI). Median nRMSE values increased as visibility radius increased, providing additional evidence that modeling visibility at shorter distances was more accurate (Table 2, Figure 5(B)). Figure 5(A) demonstrates that high biomass sites tended to have lower R^2 values, indicating that predicting visibility in areas with abundant vegetation may be less accurate. However, high biomass sites also tended to have lower nRMSE (Figure 5(B)). VI for these sites was generally very low (eg < 0.01), so while a model may have had poor predictive power (low R^2), most of the predictions were at or near zero VI, resulting in low predictive error (low nRMSE). One example of this is Site 5, where the site-scale models produced low R^2 and low nRMSE values (Figure 6). Across all radii, site-scale model R^2 and nRMSE values had significant (at an $\alpha = 0.05$ level), negative correlations with site mean biomass (Table 3, Figure A1). This suggests that low biomass sites tended to have strong predictive power (high R^2) (Figure 5(A)) and higher predictive error (high nRMSE) (Figure 5(B)), likely because these sites had a greater range of possible VI values (Table A4). SDE across all radii also had a negative relationship with model R^2, but none of the relationships were significant. Significant positive relationships were also found between mean observed VI and model R^2 as well as mean observed VI and

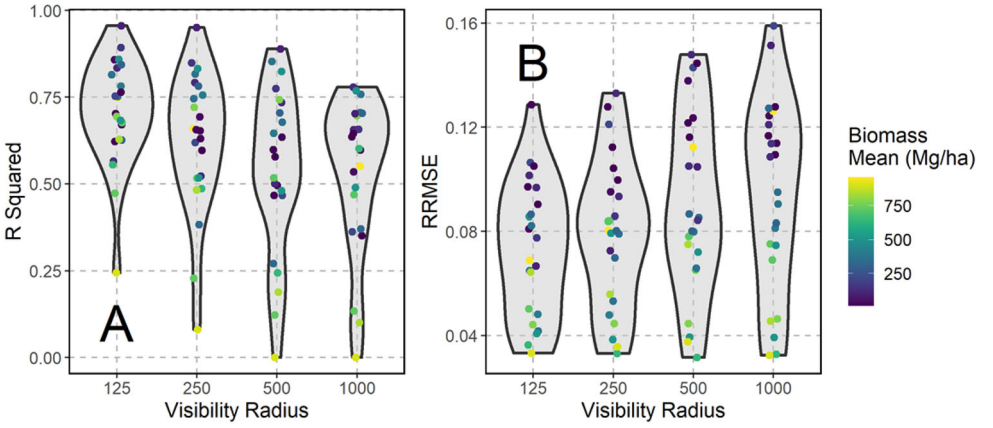

Figure 5. The 24 site-scale model R^2 (A) and nRMSE (B) values as a function of visibility radius. Points are colored by mean biomass and vertically 'jittered' using the R package ggplot2 (version 3.4.1) (Wickham 2016) to reduce overlap. Gray areas represent smoothed probability density at each radius.

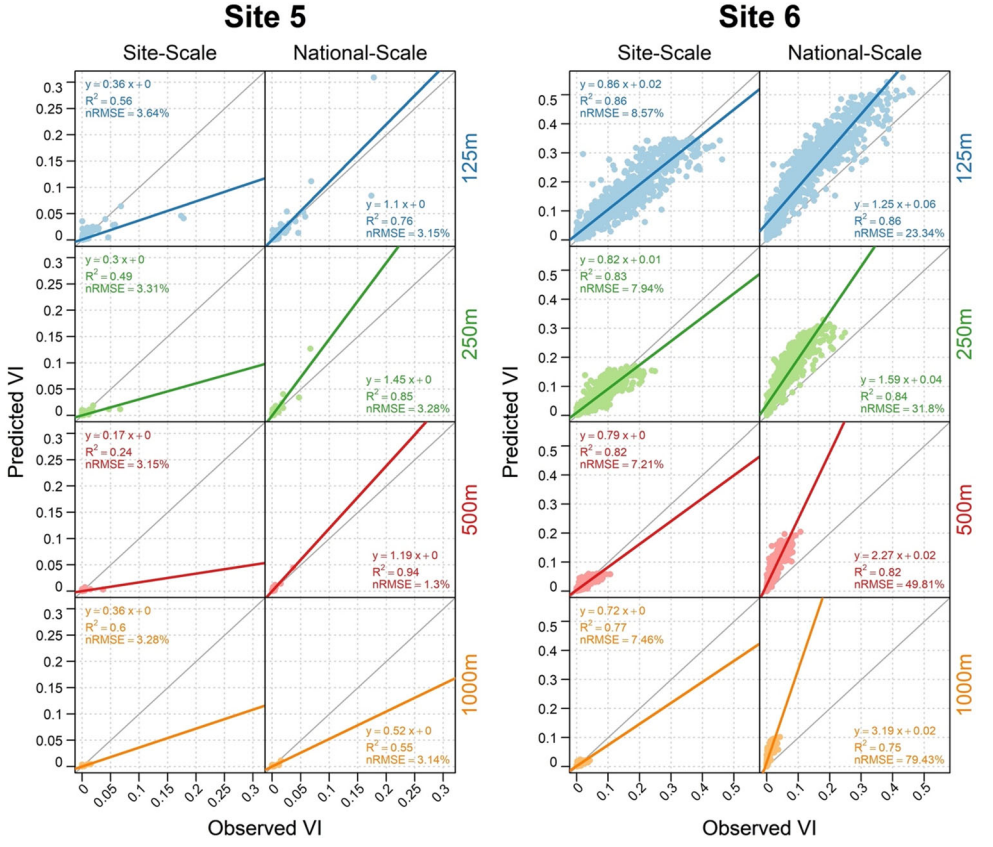

Figure 6. Predicted versus observed VI for site-scale and national-scale models at each of the four visibility radii.

Table 3. Correlation between model performance metrics and site characteristics, see Figures A1 and A2 for full scatterplots from which the correlation metrics are derived.

			Pearson's r for dependent variable:	
Visibility radius (m)	Model type	Explanatory variable	R^2	nRMSE
125	Site	Biomass	−0.48*	−0.70†
		SDE	−0.37	0.13
		Observed VI	0.648†	0.81†
	National	Biomass	−0.13	−0.51*
		SDE	−0.44*	−0.17
		Observed VI	0.23	−0.03
250	Site	Biomass	−0.48*	−0.66†
		SDE	−0.37	0.21
		Observed VI	0.64†	0.77†
	National	Biomass	−0.11	−0.37
		SDE	−0.51*	−0.14
		Observed VI	0.14	0.15
500	Site	Biomass	−0.47*	−0.69†
		SDE	−0.39	0.21
		Observed VI	0.57†	0.85†
	National	Biomass	−0.37	−0.29
		SDE	−0.58†	−0.17
		Observed VI	0.01	−0.05
1000	Site	Biomass	−0.45*	−0.69†
		SDE	−0.38	0.16
		Observed VI	0.42*	0.89†
	National	Biomass	0.06	−0.16
		SDE	−0.52†	−0.21
		Observed VI	−0.08	−0.13

Notes: Biomass and SDE were variables used in initial site selection. Observed VI was log transformed to account for a strong positive skew.
*Significant at the $p < .05$ level.
†Significant at the $p < .01$ level.

model nRMSE (Table 3). These relationships are at least partly attributable to the fact that low-visibility sites (eg closed canopy forest) had comparably little variation in VI for the models to use in building predictive relationships.

Overall, the site-scale models were most influenced by vegetation-based variables with canopy height and canopy cover within smaller focal areas (eg ch_mean_2, cc_mean_2, ch_mean_4, cc_mean_4) having the largest average increase in mean squared error (MSE) when omitted from the model (Figure 7). Vegetation-based variables accounted for 80% of the top 20 most important variables (Figure 7). The only terrain-based variables that ranked in the top 20 were TPI and mean curvature at four different radii (Figure 7). However, the top 20 most important variables for modeling the lowest biomass site (9.8 Mg/ha) were all terrain-based, again with TPI and mean curvature occupying the top 11 most important variables. Focal predictors were by far the most important (accounting for 90% of the top 20 most important variables) among the four geospatial scopes (local, focal, zonal and global), suggesting that terrain and vegetation conditions within an area surrounding an observer were of greater importance in predicting VI.

3.2. National-scale modeling

Model performance metrics were derived from a comparison between the predicted and observed VI of the validation site that was left out of model training, with 24 total

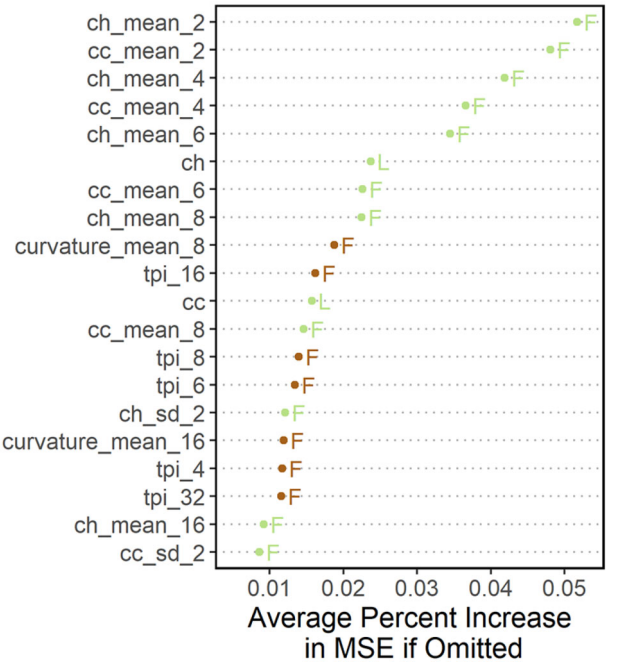

Figure 7. Variable importance averaged across all 384 site-scale models (24 regions × 4 folds × 4 radii). Green indicates vegetation-derived variables, brown indicates terrain-derived variables. Letters represent geospatial scope where L = local and F = focal. For descriptions of variable abbreviations, see Table A2.

validation sites considered per radius. This enabled a direct comparison to site-level results, with the key difference being site-level results were driven by VI data within each site whereas national-level results were driven by VI data outside of each site. Generally, the national models outperformed the site models according to R^2, across all radii except 1000 m where site-scale median R^2 was slightly higher than national-scale median R^2 (Table 2; Figure 8(A)). As with the site-scale models, shorter distances had higher median R^2 compared to longer distances (Table 2). While R^2 values broadly improved across the 24 sites, the most notable improvement was in sites that had very low site-scale R^2 values, which tended to be high in biomass and low in mean VI (Figure 8(A)). Median nRMSE values were higher at the national scale than the site scale but were still positively correlated to visibility radius (Table 2, Figure 8(B)). High nRMSE tended to occur at a small number of sites where national model bias was higher, resulting in systematic under- or overprediction of VI. Site 6 is one example of this, where the strong national-scale correlation between predictions and observations produced a high R^2 but the near-universal overprediction of VI resulted in a high nRMSE (Figure 6).

Unlike the site-scale models, there were no significant relationships between national-scale model performance (R^2 or nRMSE) and test site biomass mean, except for a lower confidence ($\alpha = 0.05$) negative correlation between biomass and nRMSE at 125 m visibility radius (Table 3, Figure A2). This further suggests that national-scale models are performing better across all biomass conditions. Unlike the site-scale models, there were no significant relationships between observed visibility and national

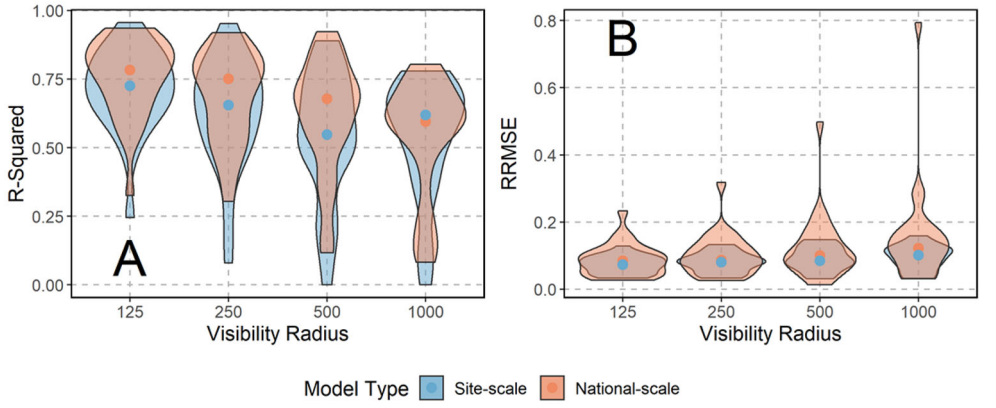

Figure 8. Comparison of site-scale and national-scale R^2 (A) and nRMSE (B). Shaded areas represent smoothed probability densities for site- and national-scale values across the 24 sites. Points indicate median values.

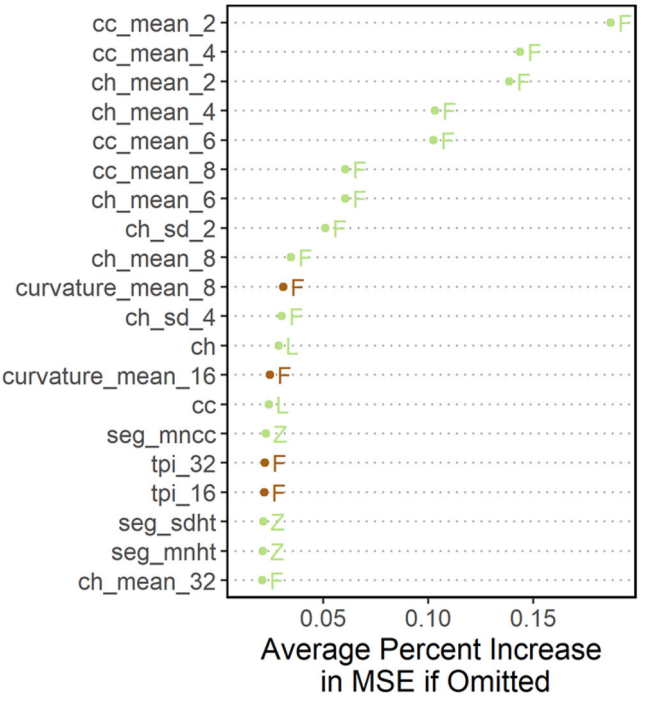

Figure 9. National-scale model variable importance, averaged across all 96 national models (24 sites × 4 radii). Green indicates vegetation-derived variables, brown indicates terrain-derived variables. Letters represent geospatial scope where L = local, Z = zonal and F = focal. For descriptions of variable abbreviations, see Table A2.

model performance (Table 3, Figure A2). This suggests that the national-scale models perform much more consistently across a range of visibility conditions than the site-scale models. The lack of correlation between model performance and visibility and

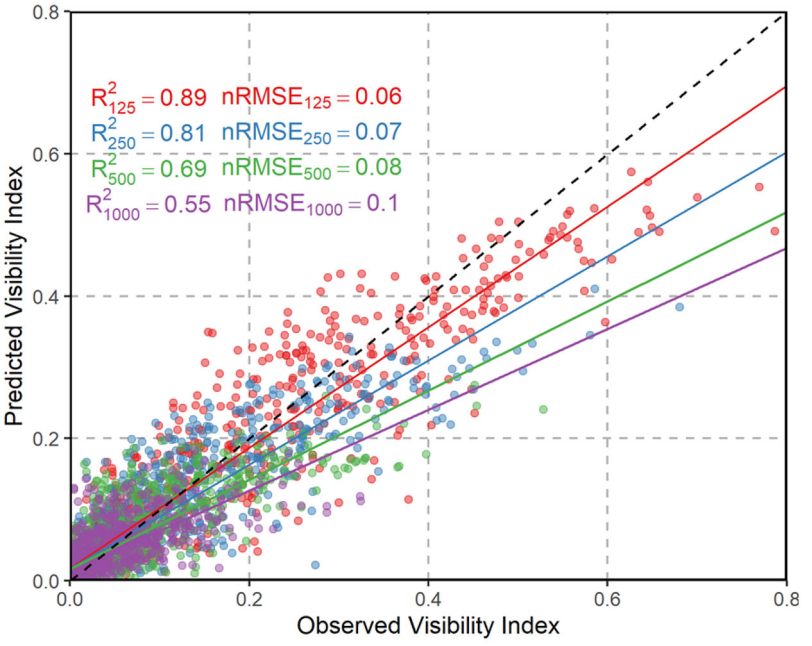

Figure 10. Predicted versus observed VI for Monroe Mountain test site. Color and subscripts refer to visibility radius.

mean biomass demonstrates that national-scale models were more robust in their performance, compared with site-scale models.

National models were most heavily-influenced by focal variables (accounting for 75% of the top 20 most important variables), bolstering the case that landscape features in one's immediate vicinity play a key role in dictating visibility (Figure 9). Unlike site-scale models, those at the national-scale relied more heavily on zonal variables (eg seg_mncc, seg_sdht, seg_mnht), suggesting that segmentation of landscape features provides greater insight into drivers of visibility at a broader scale. Some national-scale models were found to underperform, compared with site-scale models, on sites with high SDE. For example, Site 13 in New Mexico had low biomass (25.3 Mg/ha) and high SDE (145.1 m) and site-scale $R^2_{125m} = 0.70$ and $R^2_{1000m} = 0.60$, but national-scale $R^2_{125m} = 0.56$ and $R^2_{1000m} = 0.58$. Reduced national-scale R^2 is likely a result of these models' heavier reliance on vegetation-based predictors in comparison to terrain-based predictors (Figure 9). Whereas site-scale models could account for areas with complex terrain and no vegetation by upweighting terrain variables to more accurately represent local drivers of visibility, the national models were more dominated by vegetation-based predictors.

3.2.1. Monroe Mountain case study

The national-scale model trained on all 24 sites was able to predict visibility within the Monroe Mountain test site with high explanatory power at a radius of 125 m with an R^2 of 0.89 (Figure 10). Similar to the training and validation results, R^2 decreased and nRMSE increased as visibility radius increased. However, even at 1000 m the test data

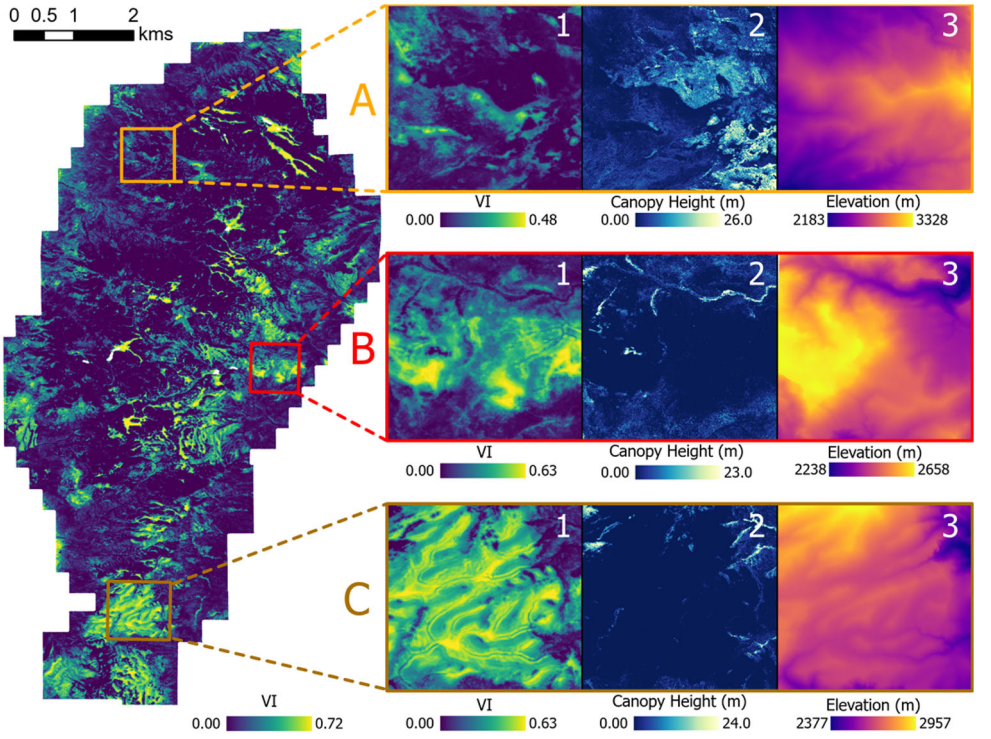

Figure 11. Monroe Mountain test site showing full map of 125 m visibility index predicted by the final national-scale model. Three insets (A, B, C) highlighting (1) 125 m visibility index predicted by the final national-scale model, (2) canopy height (m) and (3) elevation (m).

were able to be modeled with an R^2 of 0.55 and nRMSE values remained relatively low.

Mapping visibility across the entire test site revealed several pockets of high visibility (Figure 11(B1,C1)), with an overall maximum VI of 0.72 at a 125 m radius (Figure 11). Generally, areas of high visibility lacked tall vegetation (Figure 11(C2)); however, not all areas with short-to-no vegetation were modeled as having high visibility, likely due to local topography (Figure 11(A)). The insets in Figure 11 show neither canopy height nor elevation is the singular driver of visibility.

Prediction error (predicted VI – observed VI) across the Monroe Mountain site was low, with 76% of points having VI error within +/− 5% and 92% of points having VI error within +/− 10% (Figure 12(C)). Areas with high canopy cover and low visibility maintained the relatively small prediction errors (Figure 12(A)). Larger prediction errors could be found in proximity to forest edges and within some clearings with relatively low canopy cover and higher topographic variability (Figures 12(B) and A3). Modeling prediction error using the full suite of predictors revealed that, on average across radii, they could explain 21% of the variance in observed VI. This suggests that certain landscape features driving visibility in the Monroe Mountain area were not optimally emphasized by the national model, and that marginally higher accuracy could potentially be realized using a site-scale model. The Monroe Mountain area has many patches of high

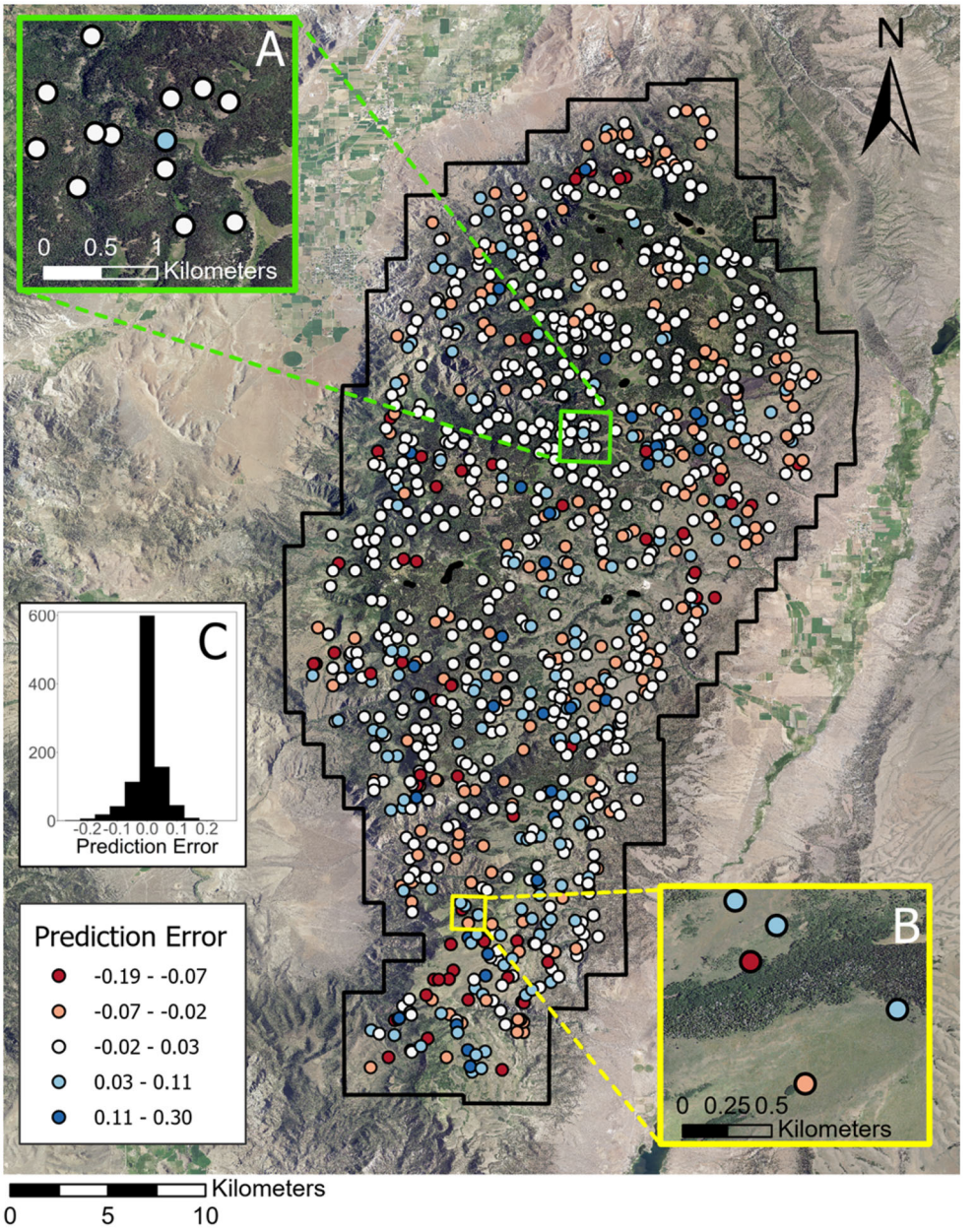

Figure 12. Prediction error at viewshed points within Monroe Mountain test site (black outline) for 125 m visibility radius. Background is 2016 NAIP imagery. (A) Inset showing a forested area with very low prediction error. (B) Inset showing area of higher prediction error. (C) Distribution of overall prediction error.

and low canopy cover, a fairly unique characteristic that may not be adequately represented by the 24 training and validation sites. Still, the national model produced very low error across an independent landscape, suggesting that a national model may predict visibility across other landscapes with low prediction error.

4. Discussion

This study presented a new method for modeling continuous visibility, across a variety of landscapes in the contiguous US, using ALS-driven random forest models that produced accurate predictions and dramatically improved processing times compared to a pixel-by-pixel viewshed-driven approach. We found that:

(1) VI derived from a high-resolution surface model can be approximated by coarser resolution landscape information.
(2) National-scale models were more accurate than site-scale models, according to R^2 values.
(3) Site-scale models had significant correlations between model performance and vegetation conditions, unlike national-scale models, suggesting that the latter are performing better across all landscape conditions.
(4) Vegetation variables were most influential in predicting visibility, especially at small focal radii.

Overall, there was a consistent relationship between model performance and visibility radius, such that shorter radii (eg 125 m) produced higher model accuracy than longer range visibility (eg 1000 m). While the human eye can see beyond 1000 m, our results suggest that the accuracy of modeling VI will decrease as viewing radius increases. The chosen range of radii balanced broad landscape-scale usefulness and processing capacity and while it could be expanded to longer distances in future work, there would likely be a reduction in accuracy at longer distances.

Our results, especially at the national-scale 125 m visibility radius (median R^2 = 0.78, median nRMSE = 8.4%), are generally in agreement with similar work done by Zong *et.al.* (2021), whose methods – despite the many differences discussed in the Introduction – resulted in a median R^2 of 0.77 and a range of nRMSE values from 11.81% to 15.92% across their different plot sizes. This further proves the usefulness of using random forest models to model visibility across landscapes, however future work may consider implementing other machine learning frameworks in lieu of random forests to determine if a superior modeling framework exists.

While previous work has demonstrated the capacity to decrease processing times associated with visibility calculations (Franklin and Ray 1994, Gao *et al.* 2011, Cauchi-Saunders and Lewis 2015, Tabik *et al.* 2015, Sanchez-Fernandez *et al.* 2021), our work outlines a new sample-based method relying on machine learning rather than the traditional brute-force approach involving calculating visibility from every possible viewpoint. While building our random forest model relied initially on a sample of viewsheds, the final map of predictions at an independent test site relied only on the previously built national-scale model. In theory, new maps of visibility at other locations could be produced without having to calculate a single additional viewshed. However, the decreases in predictive accuracy that our approach yielded at greater viewing radii demonstrates the limitations of using a sample-driven approach. These limitations would be less likely to emerge in a purely viewshed-driven approach (such as Sanchez-Fernandez et al. 2021), given that true visibility measurements are computed for every cell, rather than estimated using a predictive model. Thus, there is an

important trade-off between sample-based approaches (less accurate but likely faster) and census-based approaches (more accurate but likely slower).

Using R^2 as the primary performance metric, national-scale models demonstrated superior performance compared to site-scale models. We attribute this result to the fact that national models, trained on data from a wide range of landscape conditions across the US, captured more diversity in VI, allowing predictive models to recognize trends even in sites that featured narrow ranges of VI. At some sites VI was almost universally near zero due to the presence of consistently high vegetation cover. Because these sites featured so little variance in VI, site-scale models struggled to build robust relationships between terrain/vegetation structural metrics and VI. However, national-scale models could more easily identify these relationships, given their more diverse training dataset (eg Site 5, Figure 6). This result stands somewhat in contrast to what one might expect – commonly, models trained on local data tend to perform better at making local predictions than models trained on wide-ranging data from a variety of distant and unrelated study areas (eg Stovall et al. 2021). Importantly, this provides great promise toward the eventual goal of being able to map visibility over large areas without having to acquire local training data.

We did, however, find that site-scale models produced lower nRMSE values, on average – a result that may appear at odds with the R^2-based results. While the national model was trained on a broad range of terrain and vegetation conditions, 24 sites may not capture the full range of potential geographic conditions present within the US. Some sites featured unique geographies not present in the training data that resulted in systematic over- or underestimation of VI. This is evident in the long, high-nRMSE tail of the national model distributions in Figure 8(B) and the prediction-observation comparisons for Site 6 (Figure 6). At these sites, correlations between predictions and observations were still fairly high (leading to high R^2), but the predictions were consistently high or low relative to observations (leading to high nRMSE). Unique, site-specific characteristics may always be problematic for a national-scale model, and if less biased VI is of prime importance, then a site-scale model may be preferable. However, if capturing relative trends in VI is desired (eg 'Where is the highest visibility within a study area?'), R^2 would indicate that a national-scale model would be preferable.

The Monroe Mountain site that served as an independent evaluation of the final national model produced results similar to the training and validation results across the 24 initial sites. With an R^2 of 0.89 for 125 m visibility, the test at Monroe Mountain demonstrates the potential for application to other landscapes independent of and geographically distinct from the original 24 training and validation sites. The continuous map of visibility serves as an example of the types of maps that may be useful to an array of disciplines. Similar maps may provide useful information for habitat suitability (Johnson and Swift 2000, Pilliod *et al.* 2022), archaeology (O'Driscoll 2017, Schirru and Castangia 2022), landscape and urban planning (Labib *et al.* 2021, Nopp-Mayr *et al.* 2021), or emergency response (Pompa-Garcia 2010, Sivrikaya *et al.* 2013, Mistick *et al.* 2022) applications, among many others.

Variable importance at site and national scales highlighted the importance of focal vegetation-based metrics for predicting visibility. Both canopy height and canopy cover were consistently among the most influential variables in modeling

(predominantly the focal mean across smaller radii, with standard deviation having a lesser but still noticeable importance). Topography-based metrics were not as well represented in average importance, with curvature and TPI making up just a small percentage of the top 20 most important variables. This provides further evidence toward the fact that viewshed and visibility analyses that rely purely on terrain models are failing to capture the prevalent effects of vegetation (Guth 2009, Starek *et al.* 2020). However, low importance of topography-based metrics does not justify omitting these variables from modeling. Variable importance resulting from the site-scale modeling of our lowest biomass site showed only topography-based metrics, suggesting that some sites – particularly low biomass sites – may rely more heavily on topographic information than others. In areas devoid of vegetation, terrain is the dominant control on visibility, so even if terrain features played a comparably small role, they cannot be ignored.

Predictor variables were produced at a much coarser spatial resolution (10 m) than the resolution of the lidar raster used to calculate observed VI (1 m). Since vegetation-based metrics like canopy height are dependent on spatial resolution, visibility index model accuracy could degrade as spatial resolution coarsens. Further work is needed to determine the relationship between predictor spatial resolution and the capacity to accurately estimate VI. The 10 m spatial resolution used in our analysis was selected to be scalable to very large areas and to demonstrate predictions at a resolution at which non-lidar-dependent vegetation and terrain structural metrics can be derived (Farr and Kobrick 2000, Homer *et al.* 2012, Sugarbaker *et al.* 2014, Karlson *et al.* 2015, Vogeler *et al.* 2018, Lang *et al.* 2019, Potapov *et al.* 2021).

ALS data quality such as point density and variations in seasonal timing of data collection can affect the ability to accurately characterize terrain and vegetation structure (Estornell *et al.* 2011, Campbell *et al.* 2018, Moudrý *et al.* 2019) and generate accurate viewsheds (Aben *et al.* 2018). However, given the fact that both viewsheds and terrain/-vegetation predictors were generated using data (DSMs, DTMs, CHMs) from the same lidar point clouds, any variations in lidar quality did not affect model performance.

One important limitation of this study is the assumption that all vegetation is visibly impenetrable. While the DSMs were generated at a high spatial resolution (1 m), enabling the precise structural characterization of vegetation and terrain elevations, DSM-based approaches to viewshed modeling fail to account for the fact that one can see through and under some vegetation (Bartie *et al.* 2011, Murgoitio *et al.* 2013). Certain vegetation types, such as lodgepole pine forests in the US (Murgoitio *et al.* 2013), may promote through-stand visibility, given their high canopy base heights and lower vegetation densities in the understory. In these environments, our analysis may underestimate visibility relative to true visibility. However, vegetation in other ecosystems is naturally more opaque at or near eye-level; therefore, future work may consider the importance of vegetation type on predicting visibility. Further, a growing body of research has sought to exploit the detailed three-dimensional structural information contained within terrestrial point clouds to gain a more nuanced accounting of within-vegetation visibility (eg Bartie *et al.* 2011, Lecigne *et al.* 2020, Zong *et al.* 2021, 2022). For example, Lecigne *et al.* (2020) developed an algorithm that calculates viewsheds directly from TLS point clouds, accounting for the visually penetrable nature

of vegetation by capturing full three dimensional structures and returning the degree to which voxels are visible. However, we sought to develop an approach that did not require the use of TLS data in the interest of facilitating broad-scale VI mapping across any areas with available ALS data without having to collect field data.

Another limitation of our work, and of all efforts related to quantifying VI, is that VI is inherently directionless. Viewshed maps are valuable in that they provide a discrete and spatially-explicit accounting of portions of the landscape that can and cannot be seen from a particular vantage point. In many cases, there is a strong directional component to viewsheds (eg Figure 1). For example, if one is standing at the edge of forest clearing, their visibility will be high in the viewing direction away from the forest and low in the viewing direction into the forest. Viewsheds can make this distinction spatially, but VI, which simply summarizes proportional visibility irrespective of direction, cannot. Both VI and predictor variables could be calculated within a directionally-limited range of view azimuths, providing a potential path to modeling directional visibility. Future work should inquire into the extent to which VI estimates can be made directionally-explicit. Additionally, if directionality is germane to a particular study's objectives, modeled VI at coarser spatial resolution can still provide a path to greatly decreasing computation time. An estimated VI raster produced by a national-scale model could be used to select a limited number of locations with the desired visibility characteristics, and viewsheds could be subsequently calculated for those locations using the traditional approach.

While this study relied on lidar data for modeling visibility, the predictor variables were designed such that they could be generated from other datasets. For example, vegetation height has been mapped over broad spatial scales at 10 m and 30 m (Lang *et al.* 2019, Potapov *et al.* 2021). Canopy cover has been extensively mapped as well (Homer *et al.* 2012, Karlson *et al.* 2015, Vogeler *et al.* 2018), and digital elevation models exist at global or near global scales at a range of resolutions (Farr and Kobrick 2000, Sugarbaker *et al.* 2014). However, none of these datasets are as accurate and precise as lidar-derived products, so there remains a degree of uncertainty surrounding the potential limits to VI predictions based on these more broadly-available data. We have begun working on modeling visibility using more widely available, coarser resolution data to determine whether national- or global-scale visibility maps may be feasible.

5. Conclusion

In this study, we have introduced a computationally-efficient approach to mapping proportional visibility across large geographic extents in a spatially-exhaustive manner at 10 m spatial resolution. Our approach, (predicting VI using a random forest model trained on a sample of viewsheds) was found to speed up computation time by orders of magnitude compared to a traditional viewshed approach (calculating viewsheds from every possible raster grid cell within an area of interest), does not require the collection of field data and can potentially be applied anywhere where there are recent, high-quality ALS data. Our results demonstrated that visibility can be predicted with a high degree of accuracy, both at the site scale and at the national scale. Site-scale models benefit from the ability to tailor predictions to a set of predictor variables that are the most relevant drivers of visibility in a given area (eg canopy height may not be a useful predictor in a topographically diverse site devoid of vegetation). However, particularly

in areas of low visibility, site-scale models may not capture a sufficient range of variability for producing accurate results. National-scale models benefit from their capacity to be broadly applied and capture universal trends in drivers of visibility across a diversity of landscapes. However, as with all national-scale maps, they may struggle to capture visibility within unique landscapes not included in the training and validation data. That said, the impressive performance of our national-scale model in an independent test area highlights the robustness of the sample data used to construct our models.

Disclosure statement

No potential conflict of interest was reported by the author(s).

Funding

This work was supported by the National Science Foundation (#BCS2117433) and the 632 USDA Forest Service (#21-CS-11221636-120).

Notes on contributors

Katherine A. Mistick is a Research Associate at the Utah Remote Sensing Applications Lab at the University of Utah whose research interests include geographic information science, lidar remote sensing and geospatial modeling of wildland firefighter safety. She contributed to the conceptualization, software, data curation, formal analysis, visualization and writing.

Michael J. Campbell is a Research Assistant Professor at the University of Utah whose research interests include remote sensing of vegetation structure and function, forest and woodland ecology, change detection and time series analysis, lidar remote sensing and geospatial modeling of wildland firefighter safety. He contributed to the conceptualization, methodology, writing (review & editing), visualization and funding acquisition.

Matthew P. Thompson is a Research Forester at the Rocky Mountain Research Station, Human Dimensions Program, whose research interests include the application of principles from systems engineering, industrial engineering, risk analysis, operations research, economics and decision-making under uncertainty to complex resource management with economic and environmental objectives. He contributed to the writing (review & editing) and funding acquisition.

Philip E. Dennison is Professor and Chair in the Department of Geography at the University of Utah. He is also Director of the Utah Remote Sensing Applications Lab. His research interests include wildfire and firefighter safety, remote sensing of vegetation, imaging spectroscopy and mapping greenhouse gas emissions using remote sensing. He contributed to the conceptualization, methodology, writing (review & editing), resources and funding acquisition.

Data and codes availability statement

The data, codes and instructions that support the findings of this study are available in OSF at https://doi.org/10.17605/OSF.IO/5UGRE. Lidar data on which this analysis is based is available from the USGS 3D Elevation Program at https://www.usgs.gov/3d-elevation-program.

References

Aben, J., Pellikka, P., and Travis, J.M.J., 2018. A call for viewshed ecology: advancing our understanding of the ecology of information through viewshed analysis. *Methods in Ecology and Evolution*, 9 (3), 624–633.

Bartie, P., *et al.*, 2011. Incorporating vegetation into visual exposure modelling in urban environments. *International Journal of Geographical Information Science*, 25 (5), 851–868.
Belgiu, M. and Drăguţ, L., 2016. Random forest in remote sensing: a review of applications and future directions. *ISPRS Journal of Photogrammetry and Remote Sensing*, 114, 24–31.
Campbell, M.J., *et al.*, 2018. Quantifying understory vegetation density using small-footprint airborne lidar. *Remote Sensing of Environment*, 215, 330–342.
Campbell, M.J., *et al.*, 2020. A multi-sensor, multi-scale approach to mapping tree mortality in woodland ecosystems. *Remote Sensing of Environment*, 245, 111853.
Campbell, M.J., *et al.*, 2021. Scaled biomass estimation in woodland ecosystems: testing the individual and combined capacities of satellite multispectral and lidar data. *Remote Sensing of Environment*, 262, 112511.
Cauchi-Saunders, A.J. and Lewis, I.J., 2015. GPU enabled XDraw viewshed analysis. *Journal of Parallel and Distributed Computing*, 84, 87–93.
Chamberlain, B.C. and Meitner, M.J., 2013. A route-based visibility analysis for landscape management. *Landscape and Urban Planning*, 111, 13–24.
Chao, F., *et al.*, 2011. Parallel algorithm for viewshed analysis on a modern GPU. *International Journal of Digital Earth*, 4 (6), 471–486.
Chapi, K., *et al.*, 2017. A novel hybrid artificial intelligence approach for flood susceptibility assessment. *Environmental Modelling & Software*, 95, 229–245.
Dean, D.J. and Lizarraga-Blackard, A.C., 2007. Modeling the magnitude and spatial distribution of aesthetic impacts. *Environment and Planning B: Planning and Design*, 34 (1), 121–138.
ESRI, 2022a. How geodesic viewshed works. *ArcGIS Pro* [online]. Available from: https://pro.arcgis.com/en/pro-app/2.8/tool-reference/spatial-analyst/how-viewshed-2-works.htm [Accessed 5 July 2023].
ESRI, 2022b. Segment mean shift. *ArcGIS Pro*[online]. Available from: https://pro.arcgis.com/en/pro-app/latest/tool-reference/spatial-analyst/segment-mean-shift.htm [Accessed 5 July 2023].
Estornell, J., *et al.*, 2011. Analysis of the factors affecting LiDAR DTM accuracy in a steep shrub area. *International Journal of Digital Earth*, 4 (6), 521–538.
Farr, T.G. and Kobrick, M., 2000. Shuttle radar topography mission produces a wealth of data. *Eos, Transactions American Geophysical Union*, 81 (48), 583–585.
Fisher, P., *et al.*, 1997. Spatial analysis of visible areas from the Bronze Age cairns of Mull. *Journal of Archaeological Science*, 24 (7), 581–592.
Fishman, J., Haverkort, H., and Toma, L., 2009. Improved visibility computation on massive grid terrains. In: *Proceedings of the 17th ACM SIGSPATIAL international conference on advances in geographic information systems*. Seattle ,WA: ACM, 121–130.
Franklin, W.R. and Ray, C.K., 1994. Higher isn't necessarily better: visibility algorithms and experiments. *Advances in GIS Research*, 2, 22.
Friedl, M. and Sulla-Menashe, D., 2019. *MCD12Q1 MODIS/terra + aqua land cover type yearly L3 global 500m SIN grid V006*. Available from: https://lpdaac.usgs.gov/products/mcd12q1v006/ [Accessed 17 February 2023].
Gao, Y., *et al.*, 2011. Optimization for viewshed analysis on GPU. *In: 2011 19th International conference on geoinformatics*. Shanghai, China: IEEE, 1–5.
Goodbody, T., *et al.*, 2023. sgsR : a structurally guided sampling toolbox for LiDAR-based forest inventories. *Forestry: An International Journal of Forest Research*, cpac055. https://doi.org/10.1093/forestry/cpac055
Guth, P.L., 2009. Incorporating vegetation in viewshed and line-of-sight algorithms. *In: ASPRS/MAPPS Specialty Conference*, 16–19 November 2009. San Antonio, Texas.
Hakkenberg, C.R., *et al.*, 2018. Mapping multi-scale vascular plant richness in a forest landscape with integrated LiDAR and hyperspectral remote-sensing. *Ecology*, 99 (2), 474–487.
Hijmans, R., *et al.*, 2022. Spatial data analysis [software]. Available from: https://github.com/rspatial/terra [Accessed 17 February 2023].
Hindsley, P., Hamilton, S.E., and Morgan, O.A., 2013. Gulf views: toward a better understanding of viewshed scope in hedonic property models. *The Journal of Real Estate Finance and Economics*, 47 (3), 489–505.

Homer, C.G., Fry, J.A., and Barnes, C.A., 2012. *The national land cover database*. Reston, VA: The United States Geological Society (USGS), Report No. 2012–3020.
Inglis, N.C., *et al.*, 2022. From viewsheds to viewscapes: trends in landscape visibility and visual quality research. *Landscape and Urban Planning*, 224, 104424.
Isenburg, M., 2019. LAStools [software]. Rapidlasso. Available from: https://rapidlasso.com/LAStools/ [Accessed 17 February 2023].
Johnson, T.L. and Swift, D.M., 2000. A test of a habitat evaluation procedure for Rocky Mountain bighorn sheep. *Restoration Ecology*, 8 (4S), 47–56.
Jones, E., 2006. Using viewshed analysis to explore settlement choice: a case study of the Onondaga Iroquois. *American Antiquity*, 71 (3), 523–538.
Karlson, M., *et al.*, 2015. Mapping tree canopy cover and aboveground biomass in Sudano-Sahelian woodlands using Landsat 8 and random forest. *Remote Sensing*, 7 (8), 10017–10041.
Kucuk, O., *et al.*, 2017. Visibility analysis of fire lookout towers in the Boyabat State Forest Enterprise in Turkey. *Environmental Monitoring and Assessment*, 189 (7), 329. [InsertedFromOnline]
Labib, S.M., Huck, J.J., and Lindley, S., 2021. Modelling and mapping eye-level greenness visibility exposure using multi-source data at high spatial resolutions. *The Science of the Total Environment*, 755 (Pt 1), 143050. [InsertedFromOnline]
Lake, M.W., Woodman, P.E., and Mithen, S.J., 1998. Tailoring GIS software for archaeological applications: an example concerning viewshed analysis. *Journal of Archaeological Science*, 25 (1), 27–38.
LANDFIRE Historical Disturbance, 2023. *LANDFIRE*[online]. Available from: https://landfire.gov/hdist.php [Accessed 26 April 2023].
Lang, N., Schindler, K., and Wegner, J.D., 2019. Country-wide high-resolution vegetation height mapping with Sentinel-2. *Remote Sensing of Environment*, 233, 111347.
Lecigne, B., Eitel, J.U.H., and Rachlow, J.L., 2020. viewshed3d: an r package for quantifying 3D visibility using terrestrial lidar data. *Methods in Ecology and Evolution*, 11 (6), 733–738.
Llobera, M., 2003. Extending GIS-based visual analysis: the concept of visualscapes. *International Journal of Geographical Information Science*, 17 (1), 25–48.
McPartland, M., *et al.*, 2019. Characterizing boreal peatland plant composition and species diversity with hyperspectral remote sensing. *Remote Sensing*, 11 (14), 1685.
Melville, G. and Stone, C., 2016. Optimising nearest neighbour information—a simple, efficient sampling strategy for forestry plot imputation using remotely sensed data. *Australian Forestry*, 79 (3), 217–228.
Microsoft, 2018. US building footprints [dataset]. Available from: https://github.com/Microsoft/USBuildingFootprints [Accessed 17 February 2023].
Mistick, K.A., *et al.*, 2022. Using geographic information to analyze wildland firefighter situational awareness: impacts of spatial resolution on visibility assessment. *Fire*, 5 (5), 151.
Moudrý, V., *et al.*, 2019. Comparison of leaf-off and leaf-on combined UAV imagery and airborne LiDAR for assessment of a post-mining site terrain and vegetation structure: prospects for monitoring hazards and restoration success. *Applied Geography*, 104, 32–41.
Murgoitio, J.J., *et al.*, 2013. Improved visibility calculations with tree trunk obstruction modeling from aerial LiDAR. *International Journal of Geographical Information Science*, 27 (10), 1865–1883.
Nopp-Mayr, U., *et al.*, 2021. Novel application and validation of a method to assess visual impacts of rotating wind turbine blades within woodland areas. *PFG – Journal of Photogrammetry, Remote Sensing and Geoinformation Science*, 89 (1), 1–14.
O'Driscoll, J., 2017. Landscape prominence: examining the topographical position of Irish hillforts using a cumulative viewshed approach. *Journal of Archaeological Science: Reports*, 16, 73–89.
Olsoy, P.J., *et al.*, 2015. Fearscapes: mapping functional properties of cover for prey with terrestrial LiDAR. *BioScience*, 65 (1), 74–80.
Otgonbayar, M., *et al.*, 2019. Mapping pasture biomass in Mongolia using partial least squares, random forest regression and Landsat 8 imagery. *International Journal of Remote Sensing*, 40 (8), 3204–3226.
Palmer, J.F., 2008. The perceived scenic effects of clearcutting in the White Mountains of New Hampshire, USA. *Journal of Environmental Management*, 89 (3), 167–183. [InsertedFromOnline]
Parsons, B.M., *et al.*, 2020. Building a perceptual zone of influence for wildlife: delineating the effects of roads on grizzly bear movement. *European Journal of Wildlife Research*, 66 (4), 53.

Pilliod, D.S., *et al.*, 2022. Leveraging rangeland monitoring data for wildlife: from concept to practice. *Rangelands*, 44 (1), 87–98.

Pompa-Garcia, M., 2010. Viewshed analysis for improving the effectiveness of watchtowers, in the north of Mexico∼!2010-03-06∼!2010-06-14∼!2010-07-26∼!. *The Open Forest Science Journal*, 3 (1), 17–22.

Potapov, P., *et al.*, 2021. Mapping global forest canopy height through integration of GEDI and Landsat data. *Remote Sensing of Environment*, 253, 112165.

PRISM Climate Group, 2022. Oregon State University. Available from: https://prism.oregonstate.edu [Accessed 28 April 2023].

Probst, P., *et al.*, 2019. Hyperparameters and tuning strategies for random forest. *WIREs Data Mining and Knowledge Discovery,* 9, e1301.

Qarah, F.F., 2020. Efficient viewshed computation algorithms on GPUs and CPUs. Thesis (PhD). University of South Florida. USF Tampa Graduate Theses and Dissertations.

Roberts, D.R., *et al.*, 2017. Cross-validation strategies for data with temporal, spatial, hierarchical, or phylogenetic structure. *Ecography*, 40 (8), 913–929.

Sahraoui, Y., *et al.*, 2018. Integrated GIS software for computing landscape visibility metrics. *Transactions in GIS*, 22 (5), 1310–1323.

Sanchez-Fernandez, A.J., *et al.*, 2021. A data relocation approach for terrain surface analysis on multi-GPU systems: a case study on the total viewshed problem. *International Journal of Geographical Information Science*, 35 (8), 1500–1520.

Sander, H.A. and Polasky, S., 2009. The value of views and open space: estimates from a hedonic pricing model for Ramsey County, Minnesota, USA. *Land Use Policy*, 26 (3), 837–845.

Schirru, D. and Castangia, G., 2022. All along the watchtower: visibility analysis on Bronze Age Sardinian megalithic landscapes. *Journal of Archaeological Science: Reports*, 43, 103437.

Sivrikaya, F., *et al.*, 2013.Evaluation of forest fire risk with GIS. *Polish Journal of Environmental Studies*, 23, 187–194.

Spawn, S.A., *et al.*, 2020. Harmonized global maps of above and belowground biomass carbon density in the year 2010. *Scientific Data*, 7 (1), 112. [InsertedFromOnline]

Starek, M.J., *et al.*, 2020. Viewshed simulation and optimization for digital terrain modelling with terrestrial laser scanning. *International Journal of Remote Sensing*, 41 (16), 6409–6426.

Stojanovic, N. and Stojanovic, D., 2013. Performance improvement of viewshed analysis using GPU. *In: 2013 11th international conference on telecommunications in Modern Satellite, Cable and Broadcasting Services (TELSIKS)*. Nis, Serbia: IEEE, 397–400.

Stovall, A.E.L., *et al.*, 2021. Comprehensive comparison of airborne and spaceborne SAR and LiDAR estimates of forest structure in the tallest mangrove forest on earth. *Science of Remote Sensing*, 4, 100034.

Sugarbaker, C., *et al.*, 2014. *The 3D elevation program initiative—a call for action*. Reston, VA: U.S. Geological Survey.

Tabik, S., *et al.*, 2015. Efficient data structure and highly scalable algorithm for total-viewshed computation. *IEEE Journal of Selected Topics in Applied Earth Observations and Remote Sensing*, 8 (1), 304–310.

Tabik, S., Zapata, E.L., and Romero, L.F., 2013. Simultaneous computation of total viewshed on large high resolution grids. *International Journal of Geographical Information Science*, 27 (4), 804–814.

van Kreveld, M., 1996. *Variations on sweep algorithms*. Department of Computer Science, Utrecht, Netherlands: Utrecht University.

Vogeler, J.C., *et al.*, 2018. Extracting the full value of the Landsat archive: inter-sensor harmonization for the mapping of Minnesota forest canopy cover (1973–2015). *Remote Sensing of Environment*, 209, 363–374.

Vukomanovic, J., *et al.*, 2018. Not seeing the forest for the trees: modeling exurban viewscapes with LiDAR. *Landscape and Urban Planning*, 170, 169–176.

Weiss, A., 2001. Topographic position and landforms analysis. *In: ESRI User Conference*. San Diego, California, USA.

Wheatley, D., 1995. Cumulative viewshed analysis: a GIS-based method for investigating intervisibility, and its archaeological application. *In:* G. Lock and Z. Stancic, eds. *Archaeology and GIS: a European perspective*. London: Routlege, 171–185.

Wheatley, D. and Gillings, M., 2000. Vision, perception and GIS: some notes on the development of enriched approaches to the study of archaeological visibility. *In:* G. Lock, ed. *Beyond the map archaeology and spatial technologies*. Oxford, UK: IOS Press, 1–27.

Wickham, H., 2016. *ggplot2: elegant graphics for data analysis [software]*. New York, NY: Springer-Verlag.

Wright, M., Wager, S., and Probst, P., 2022. *A fast implementation of random forests* [software]. Available from: https://github.com/imbs-hl/ranger [Accessed 17 February 2023].

Wyse, S.V., Hulme, P.E., and Etherington, T.R., 2022. Combining laser rangefinder and viewshed technologies to improve ground surveys of invasive tree distributions. *Methods in Ecology and Evolution*, 13 (3), 734–742.

Yu, S., *et al.*, 2016. View-based greenery: a three-dimensional assessment of city buildings' green visibility using Floor Green View Index. *Landscape and Urban Planning*, 152, 13–26.

Zhang, Y., Liu, J., and Shen, W., 2022. A review of ensemble learning algorithms used in remote sensing applications. *Applied Sciences*, 12 (17), 8654.

Zhao, Y., Padmanabhan, A., and Wang, S., 2013. A parallel computing approach to viewshed analysis of large terrain data using graphics processing units. *International Journal of Geographical Information Science*, 27 (2), 363–384.

Zong, X., *et al.*, 2021. Estimating fine-scale visibility in a temperate forest landscape using airborne laser scanning. *International Journal of Applied Earth Observation and Geoinformation*, 103, 102478.

Zong, X., *et al.*, 2022. LiDAR reveals a preference for intermediate visibility by a forest-dwelling ungulate species. *Journal of Animal Ecology*, 92, 1306–1319.

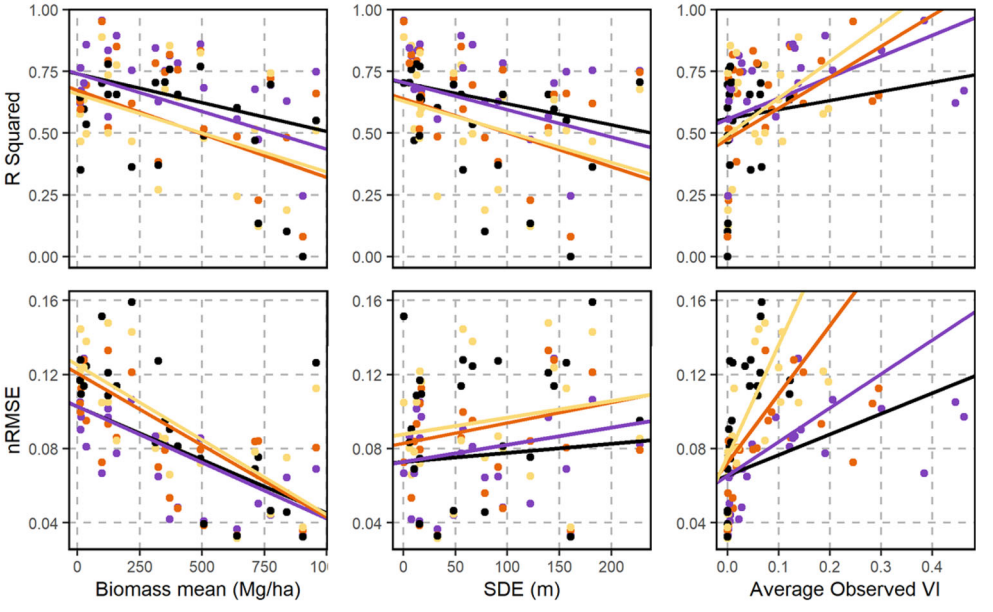

Figure A1. Scatterplots showing regressions between site-scale model performance metrics (y-axes) and site characteristics (x-axes), whose correlation coefficients are summarized in Table 3. Color refers to visibility radius (black = 125, purple = 250, orange = 500, yellow = 1000).

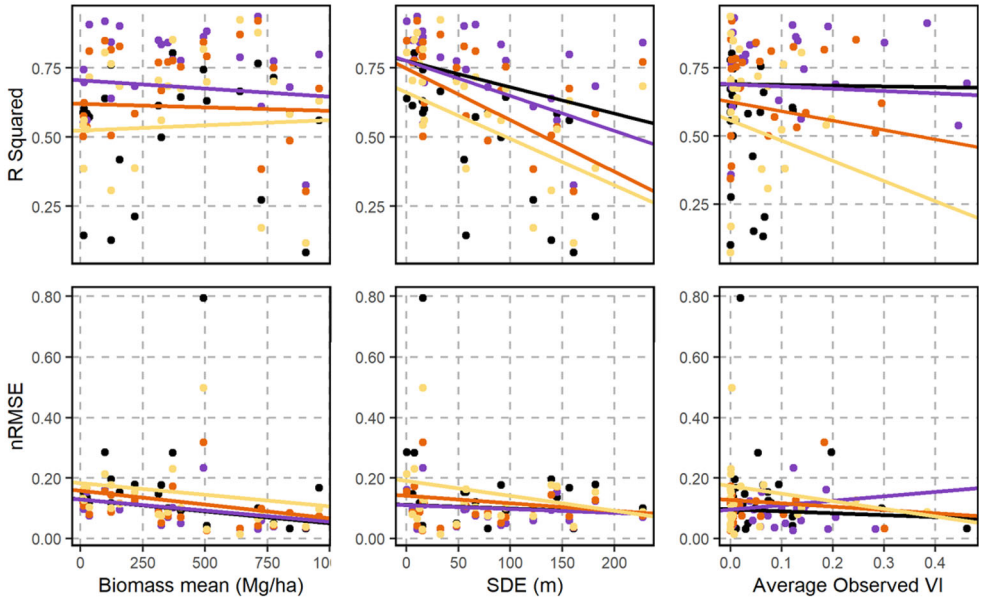

Figure A2. Scatterplots showing regressions between national-scale model performance metrics (y-axes) and site characteristics (x-axes), whose correlation coefficients are summarized in Table 3. Color refers to visibility radius (black = 125, purple = 250, orange = 500, yellow = 1000).

Appendix A

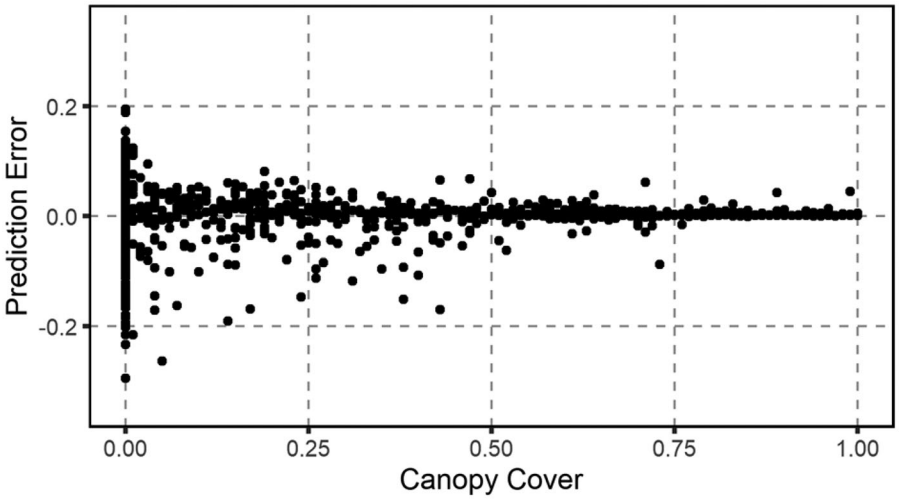

Figure A3. Scatterplot showing canopy cover and prediction error at the Monroe Mountain test site. Generally, areas with low canopy cover saw greater prediction error.

Table A1. Summary of lidar datasets used for each site.

Site	Dataset name	Collection start date	Collection end date	Pulse density (pulses/m^2)	USGS quality level
1	NH Umbagog 2016	06 April 2016	24 May 2018	5.9	QL1
2	KS Statewide B18 2018	23 January 2018	18 November 2018	3.2	QL2
3	WI Sawyer 2017	21 April 2017	22 April 2017	5.4	QL2
4	NY FEMA R2 Northeast 2017	06 May 2018	09 May 2018	5.1	QL2
5	ME Eastern B1 2017	30 April 2017	04 December 2017	4.1	QL2
6	MI FEMA Luce Schoolcraft 2019	2020 May 13	20 May 2020	3.2	QL2
7	UT Statewide South 3 2020	06 May 2020	23 August 2020	4.4	QL2
8	WA EasternCascades 5 2019	03 November 2019	14 2020 August	11.7	QL1
9	WY Southwest 1 2020	11 August 2020	25 August 2020	4.6	QL2
10	SD NRCS QSI A4 2017	20 April 2017	24 April 2017	7.1	QL2
11	WY SouthCentral 5 2020	2020 August 28 2020	13 October 2020	30.6	QL1
12	CO SanLuisJuanMiguel 5 2020	28 May 2020	04 October 2020	5.0	QL2
13	NW SouthCentral B4 2018	20 November 2018	27 May 2019	4.3	QL2
14	CA SoCAL Wildfires B3 2018	27 May 2018	22 July 2018	5.3	QL2
15	CO Southwest NRCS B3 2018	05 October 2018	24 September 2019	13.4	QL2
16	OK Woodward UTM14 B2 2016	13 December 2016	17 April 2017	3.9	QL2
17	CO NESE Colorado 2 2019	2019 August 12	05 October 2019	5.4	QL2
18	NM NorthWest Navajo A TL 2018	14 November 2018	28 November 2018	5.0	QL2
19	GA Statewide B2 2018	28 January 2019	24 April 2019	3.0	QL2
20	GA Central 1 2018	28 November 2018	28 January 2020	3.7	QL2
21	FL Southwest B 2018	08 May 2018	29 October 2018	14.5	QL1
22	KY FluorsparDistrict 2019	05 December 2019	08 February 2020	3.6	QL2
23	AL 17 Co 2 2020	10 December 2020	17 January 2021	4.3	QL2
24	NC phase 5 Swain 2017	13 March 2017	10 April 2017	64.6	QL1

Table A2. Summary of predicator variables used in modeling with abbreviations matching those used in Figures 7 and 10.

Predictor variable	Abbreviation	Description	Scope	Category
Elevation	elevation	Elevation value derived from 10 m DTM	Local	Terrain
Elevation mean	elev_mean_x	Focal mean of elevation with radius x pixels for x in [2, 4, 6, 8, 16 and 32].	Focal	Terrain
Elevation standard deviation	elev_sd_x	Focal standard deviation of elevation with radius x pixels for x in [2, 4, 6, 8, 16 and 32].	Focal	Terrain
Slope	slope	Rate of change of elevation (steepness) derived from 10 m DTM	Local	Terrain
Slope mean	slope_mean_x	Focal mean of slope with radius x pixels for x in [2, 4, 6, 8, 16 and 32].	Focal	Terrain
Slope standard deviation	slope_sd_x	Focal standard deviation of slope with radius x pixels for x in [2, 4, 6, 8, 16 and 32].	Focal	Terrain
Slope derivative	slope_deriv	Rate of change of slope derived from 10 m DTM	Local	Terrain
Slope derivative mean	slope_deriv_mean_x	Focal mean of slope derivative with radius x pixels for x in [2, 4, 6, 8, 16 and 32].	Focal	Terrain
Slope derivative standard deviation	slope_deriv_sd_x	Focal standard deviation of slope derivative with radius x pixels for x in [2, 4, 6, 8, 16 and 32].	Focal	Terrain

(*continued*)

Table A2. Continued.

Predictor variable	Abbreviation	Description	Scope	Category
Aspect sine	aspect_sin	The degree of 'east-ness' where a maximum value of 1 indicates east-facing and a minimum value of −1 indicates west-facing.	Local	Terrain
Aspect sine mean	aspect_sin_mean_x	Focal mean of aspect sine with radius x pixels for x in [2, 4, 6, 8, 16 and 32].	Focal	Terrain
Aspect sine standard deviation	aspect_sin_sd_x	Focal standard deviation of aspect sine with radius x pixels for x in [2, 4, 6, 8, 16 and 32].	Focal	Terrain
Aspect cosine	aspect_cos	The degree of 'north-ness' where a maximum value of 1 indicates north-facing and a minimum value of −1 indicates south-facing.	Local	Terrain
Aspect cosine mean	aspect_cos_mean_x	Focal mean of aspect cosine with radius x pixels for x in [2, 4, 6, 8, 16 and 32].	Focal	Terrain
Aspect cosine standard deviation	aspect_cos_sd_x	Focal standard deviation of aspect cosine with radius x pixels for x in [2, 4, 6, 8, 16 and 32].	Focal	Terrain
Slope-aspect sine	slope_aspect_sin	The product of slope and aspect sine, designed to capture 'east-ness', while down-weighting relatively flat areas and enhancing relatively steep areas.	Local	Terrain
Slope-aspect sine mean	slope_aspect_sin_mean_x	Focal mean of slope-aspect sine with radius x pixels for x in [2, 4, 6, 8, 16 and 32].	Focal	Terrain
Slope-aspect sine standard deviation	slope_aspect_sin_sd_x	Focal standard deviation of slope-aspect sine with radius x pixels for x in [2, 4, 6, 8, 16 and 32].	Focal	Terrain
Slope-aspect cosine	slope_aspect_cos	The product of slope and aspect sine, designed to capture 'east-ness', while down-weighting relatively flat areas and enhancing relatively steep areas.	Local	Terrain
Slope-aspect cosine mean	slope_aspect_cos _mean_x	Focal mean of slope-aspect cosine with radius x pixels for x in [2, 4, 6, 8, 16 and 32].	Focal	Terrain
Slope-aspect cosine standard deviation	slope_aspect_cos_sd_x	Focal standard deviation of slope-aspect cosine with radius x pixels for x in [2, 4, 6, 8, 16 and 32].	Focal	Terrain
Curvature	curvature	Curvature calculated on the 10 m DTM on a pixel-by-pixel basis according to the eight surrounding neighbors	Local	Terrain
Curvature mean	curvature_mean_x	Focal mean of curvature with radius x pixels for x in [2, 4, 6, 8, 16 and 32].	Focal	Terrain

(*continued*)

Table A2. Continued.

Predictor variable	Abbreviation	Description	Scope	Category
Curvature standard deviation	curvature_sd_x	Focal standard deviation of curvature with radius x pixels for x in [2, 4, 6, 8, 16 and 32].	Focal	Terrain
Curvature plan	curvature_plan	Curvature in the direction perpendicular to maximum slope	Local	Terrain
Curvature profile	curvature_profile	Curvature in the direction of maximum slope	Local	Terrain
Topographic position index (TPI)	tpi_x	Relative elevation, derived according to an annulus surrounding a point, with defined inner x/2 and outer radii x for x in [2, 4, 6, 8, 16, 32] (Weiss 2001)	Focal	Terrain
Canopy cover (CC)	cc	Metric describing vegetation density, calculated as the percentage of 1 m pixels with vegetation heights over 2 m within aggregated 10 m pixel area	Local	Vegetation
Canopy cover mean	cc_mean_x	Focal mean of canopy cover with radius x pixels for x in [2, 4, 6, 8, 16 and 32].	Focal	Vegetation
Canopy cover standard deviation	cc_sd_x	Focal standard deviation of canopy cover with radius x pixels for x in [2, 4, 6, 8, 16 and 32].	Focal	Vegetation
Canopy height (CH)	ch	Height of vegetation above the surface, derived from 10 m CHM.	Local	Vegetation
Canopy height mean	ch_mean_x	Focal mean of canopy height with radius x pixels for x in [2, 4, 6, 8, 16 and 32].	Focal	Vegetation
Canopy height standard deviation	ch_sd_x	Focal standard deviation of canopy height with radius x pixels for x in [2, 4, 6, 8, 16 and 32].	Focal	Vegetation
Segmented canopy height mean	seg_mnht	Mean height of segmented canopy height	Zonal	Vegetation
Segmented canopy height standard deviation	seg_sdht	Standard deviation of segmented canopy height	Zonal	Vegetation
Segment size	seg_size	Segment size of canopy height segment	Zonal	Vegetation
Segment compactness	seg_comp	Compactness of canopy height segment	Zonal	Vegetation
Segmented canopy cover mean	seg_mncc	Mean height of segmented canopy cover	Zonal	Vegetation
Segmented canopy cover standard deviation	seg_sdcc	Standard deviation of segmented canopy cover	Zonal	Vegetation
Distance to forest	seg_d2tree	Distance to nearest tree, calculated as accumulated distance to a segment with mean canopy height $\geq$ 2 m.	Global	Vegetation
Distance to clearing	seg_d2open	Distance to nearest clearing, calculated as accumulated distance to a segment with mean canopy height $<$ 2 m.	Global	Vegetation

Table A3. Summary of hyperparameters used in local modeling.

Site	Visibility radius	mtry	Minimum node	Sample fraction
1	125	87	16	0.3922208
1	250	42	4	0.3572937
1	500	6	6	0.8500453
1	1000	22	2	0.8956246
2	125	67	2	0.8677242
2	250	41	2	0.896949
2	500	84	2	0.8490319
2	1000	20	3	0.8588589
3	125	59	6	0.6847182
3	250	30	2	0.7901344
3	500	24	2	0.8910706
3	1000	33	2	0.8694142
4	125	15	2	0.7572997
4	250	12	2	0.8719646
4	500	11	2	0.8590565
4	1000	14	2	0.8903354
5	125	126	2	0.8956859
5	250	33	2	0.8971066
5	500	127	2	0.8956309
5	1000	31	10	0.8692783
6	125	62	2	0.8401027
6	250	35	2	0.7919344
6	500	24	2	0.8959702
6	1000	14	2	0.893316
7	125	45	3	0.8866096
7	250	28	2	0.8890775
7	500	22	2	0.8922536
7	1000	29	3	0.8754808
8	125	47	2	0.7693361
8	250	34	3	0.8294339
8	500	25	3	0.8912013
8	1000	33	5	0.8844946
9	125	36	2	0.8765147
9	250	25	2	0.8948843
9	500	70	2	0.8538757
9	1000	29	2	0.7871462
10	125	59	3	0.8403822
10	250	40	2	0.8968215
10	500	93	2	0.8830722
10	1000	105	2	0.8959829
11	125	36	5	0.869242
11	250	26	2	0.8022546
11	500	22	3	0.8725041
11	1000	28	2	0.8655543
12	125	51	4	0.877519
12	250	44	3	0.8070093
12	500	25	4	0.862699
12	1000	72	4	0.8355278
19	125	65	3	0.5227165
19	250	106	2	0.2213255
19	500	20	2	0.798396
19	1000	26	2	0.833453
20	125	66	2	0.7353243
20	250	17	3	0.8218555
20	500	13	2	0.8270835
20	1000	10	2	0.8560917
21	125	36	2	0.6712375
21	250	52	2	0.799502
21	500	67	2	0.8484888
21	1000	71	4	0.8930487
22	125	24	2	0.8315354

(*continued*)

Table A3. Continued.

Site	Visibility radius	mtry	Minimum node	Sample fraction
22	250	23	2	0.7820119
22	500	23	2	0.7151937
22	1000	16	2	0.8154879
23	125	38	2	0.8720128
23	250	30	2	0.8950507
23	500	62	3	0.8980366
23	1000	71	2	0.8701863
24	125	146	9	0.341819
24	250	144	5	0.2908651
24	500	121	131	0.245984
24	1000	129	85	0.2029855
13	125	65	2	0.8226684
13	250	37	3	0.8788999
13	500	46	3	0.8933841
13	1000	38	2	0.8941363
14	125	38	4	0.8718092
14	250	36	3	0.882612
14	500	22	2	0.8921064
14	1000	56	2	0.8787552
15	125	55	2	0.8492914
15	250	43	2	0.8976967
15	500	44	2	0.8917132
15	1000	35	2	0.8921256
16	125	55	2	0.7888848
16	250	64	3	0.8404448
16	500	91	5	0.8554722
16	1000	63	2	0.8891268
17	125	25	3	0.8544691
17	250	30	2	0.8753437
17	500	24	2	0.8924092
17	1000	49	2	0.8553929
18	125	17	2	0.88636
18	250	19	2	0.8607471
18	500	27	2	0.8555644
18	1000	43	2	0.8128176

Table A4. Summary of all model performance and site-specific variables.

Site	US state Coordinates	Biomass (mg/Ha)	SDE (m)	Vegetation type	Radius	Mean observed VI	Site R^2	National R^2	Site nRMSE	National nRMSE
1	ME	726.2	122.21	Closed tree canopy	125	0.004	0.47	0.61	0.05	0.06
	70.96W 44.35 N				250	0.001	0.23	0.38	0.08	0.10
					500	0.001	0.12	0.17	0.07	0.07
					1000	0.001	0.13	0.27	0.08	0.07
2	KS	122.84	12.88	Herb, grassland	125	0.301	0.84	0.84	0.10	0.10
	96.49W				250	0.183	0.79	0.82	0.09	0.09
	39.52N				500	0.103	0.73	0.76	0.11	0.10
					1000	0.059	0.78	0.76	0.11	0.12
3	WI	370.76	7.85	Closed tree canopy	125	0.022	0.81	0.78	0.04	0.10
	90.89W				250	0.01	0.82	0.78	0.05	0.17
	45.82N				500	0.005	0.85	0.85	0.07	0.23
					1000	0.002	0.76	0.80	0.09	0.28
4	NY	775.48	48.36	Closed tree canopy	125	0.005	0.69	0.78	0.04	0.04
	74.86W				250	0.002	0.72	0.75	0.04	0.04
	43.47N				500	0.001	0.74	0.70	0.04	0.05
					1000	0.000	0.70	0.67	0.05	0.05
5	ME	641.16	32.81	Closed tree canopy	125	0.000	0.56	0.76	0.04	0.03
	69.02W				250	0.000	0.49	0.85	0.03	0.03
	46.06N				500	0.000	0.24	0.94	0.03	0.01
					1000	0.000	0.6	0.56	0.03	0.03
6	MI	493.6	16.21	Closed tree canopy	125	0.127	0.86	0.86	0.09	0.23
	85.22W				250	0.050	0.83	0.84	0.08	0.32
	46.54N				500	0.017	0.82	0.82	0.07	0.50
					1000	0.006	0.77	0.75	0.07	0.79
7	UT	35.76	66.55	Open tree canopy	125	0.121	0.86	0.91	0.08	0.07
	113.78W				250	0.079	0.69	0.81	0.10	0.08
	38.01N				500	0.053	0.50	0.72	0.14	0.10
					1000	0.034	0.53	0.58	0.12	0.12
8	WA	957.68	156.95	Closed tree canopy	125	0.029	0.75	0.80	0.07	0.06
	121.00W				250	0.019	0.66	0.68	0.08	0.07
	47.71N				500	0.013	0.51	0.64	0.11	0.10
					1000	0.010	0.55	0.56	0.13	0.17
9	WY	350.56	227.43	Closed tree canopy	125	0.048	0.75	0.84	0.08	0.07
	110.67W				250	0.023	0.75	0.77	0.08	0.07
	42.90N				500	0.013	0.68	0.68	0.09	0.09
					1000	0.008	0.71	0.69	0.10	0.10

(*continued*)

Table A4. Continued.

Site	US state Coordinates	Biomass (mg/Ha)	SDE (m)	Vegetation type	Radius	Mean observed VI	Site R^2	National R^2	Site nRMSE	National nRMSE
10	SD	14.28	17.27	Herb, grassland	125	0.461	0.67	0.69	0.10	0.11
	100.42W				250	0.295	0.65	0.62	0.11	0.12
	45.22N				500	0.197	0.60	0.56	0.12	0.13
					1000	0.121	0.64	0.60	0.11	0.11
11	WY	401.64	95.5	Closed tree canopy	125	0.027	0.78	0.77	0.05	0.05
	107.09W				250	0.011	0.76	0.75	0.05	0.07
	41.10N				500	0.006	0.65	0.68	0.08	0.10
					1000	0.004	0.66	0.65	0.08	0.09
12	CO	123.68	139.65	Open tree canopy	125	0.094	0.57	0.63	0.10	0.09
	108.96W				250	0.074	0.52	0.50	0.13	0.14
	38.44N				500	0.073	0.50	0.31	0.15	0.18
					1000	0.064	0.66	0.13	0.12	0.20
13	NM	25.28	145.07	Open tree canopy	125	0.138	0.70	0.56	0.13	0.15
	108.75W				250	0.129	0.66	0.53	0.13	0.17
	31.56N				500	0.100	0.64	0.52	0.12	0.17
					1000	0.058	0.6	0.59	0.11	0.14
14	CA	156.6	55.57	Shrubland	125	0.191	0.89	0.90	0.08	0.10
	119.06W				250	0.123	0.85	0.83	0.09	0.11
	34.63N				500	0.073	0.77	0.68	0.08	0.11
					1000	0.043	0.66	0.43	0.11	0.15
15	CO	217.24	181.61	Closed Tree Canopy	125	0.206	0.75	0.69	0.11	0.12
	107.48W				250	0.147	0.62	0.58	0.12	0.13
	37.56N				500	0.107	0.47	0.38	0.14	0.15
					1000	0.066	0.36	0.20	0.16	0.18
16	OK	9.88	16.09	Herb, grassland	125	0.445	0.62	0.54	0.11	0.12
	99.78W				250	0.283	0.63	0.51	0.10	0.12
	35.09N				500	0.186	0.58	0.54	0.12	0.13
					1000	0.122	0.65	0.59	0.12	0.12
17	CO	12.6	57.62	Shrubland	125	0.143	0.76	0.75	0.09	0.10
	103.68W				250	0.086	0.6	0.57	0.10	0.11
	37.45N				500	0.061	0.47	0.38	0.14	0.16
					1000	0.045	0.35	0.15	0.13	0.15
18	NM	325	90.99	Open Tree Canopy	125	0.038	0.63	0.83	0.06	0.04
	108.88W				250	0.017	0.38	0.68	0.07	0.05
	36.02N				500	0.009	0.27	0.56	0.09	0.08
					1000	0.005	0.37	0.50	0.13	0.18

(*continued*)

Table A4. Continued.

Site	US state Coordinates	Biomass (mg/Ha)	SDE (m)	Vegetation type	Radius	Mean observed VI	Site R^2	National R^2	Site nRMSE	National nRMSE
19	GA	839.32	78.53	Closed tree canopy	125	0.003	0.63	0.68	0.06	0.07
	84.51W				250	0.001	0.48	0.5	0.06	0.08
	34.95N				500	0.000	0.19	0.59	0.08	0.08
					1000	0.000	0.10	0.59	0.05	0.03
20	GA	712.68	10.6	Open tree canopy	125	0.008	0.68	0.93	0.07	0.03
	83.51W				250	0.003	0.52	0.92	0.08	0.04
	33.22N				500	0.001	0.52	0.87	0.08	0.06
					1000	0.000	0.47	0.78	0.07	0.10
21	FL	97.36	0.47	Herb, grassland	125	0.384	0.96	0.91	0.07	0.16
	81.29W				250	0.245	0.95	0.85	0.07	0.15
	26.10N				500	0.139	0.89	0.81	0.10	0.21
					1000	0.065	0.70	0.66	0.15	0.28
22	KY	506.88	15.69	Closed tree canopy	125	0.005	0.68	0.88	0.04	0.03
	88.05W				250	0.002	0.52	0.78	0.04	0.03
	36.71N				500	0.000	0.48	0.7	0.04	0.03
					1000	0.000	0.49	0.61	0.04	0.04
23	AL	312.6	5.76	Open tree canopy	125	0.131	0.84	0.85	0.09	0.10
	86.63W				250	0.057	0.78	0.77	0.08	0.09
	32.17N				500	0.020	0.70	0.70	0.08	0.08
					1000	0.006	0.70	0.61	0.08	0.15
24	NC	905.36	160.62	Closed tree canopy	125	0.000	0.24	0.36	0.03	0.04
	83.58W				250	0.000	0.08	0.34	0.04	0.04
	35.53N				500	0.000	0.00	0.07	0.04	0.04
					1000	0.000	0.00	0.10	0.03	0.03

Note: Vegetation type comes from LANDFIRE existing vegetation type.